

Evaluation of local similarity theory in the wintertime nocturnal boundary layer over heterogeneous surface

Babić, Karmen; Rotach, Mathias W.; Bencetić Klaić, Zvezdana

Source / Izvornik: **Agricultural and Forest Meteorology, 2016, 228-229, 164 - 179**

Journal article, Accepted version

Rad u časopisu, Završna verzija rukopisa prihvaćena za objavljivanje (postprint)

<https://doi.org/10.1016/j.agrformet.2016.07.002>

Permanent link / Trajna poveznica: <https://um.nsk.hr/um:nbn:hr:217:291336>

Rights / Prava: [In copyright](#) / [Zaštićeno autorskim pravom.](#)

Download date / Datum preuzimanja: **2024-11-27**



Repository / Repozitorij:

[Repository of the Faculty of Science - University of Zagreb](#)



**Evaluation of Local Similarity Theory in the Wintertime Nocturnal Boundary Layer over
Heterogeneous Surface**

Karmen Babić¹, Mathias W. Rotach² and Zvezdana B. Klaić¹

¹ *Department of Geophysics, Faculty of Science, University of Zagreb, Zagreb, Croatia.*

² *Institute of Atmospheric and Cryospheric Sciences, University of Innsbruck, Innsbruck, Austria.*

Abstract: The local scaling approach was examined based on the multi-level measurements of atmospheric turbulence in the wintertime (December 2008– February 2009) stable atmospheric boundary layer (SBL) established over a heterogeneous surface influenced by mixed agricultural, industrial and forest surfaces. The heterogeneity of the surface was characterized by spatial variability of both roughness and topography. Nieuwstadt's local scaling approach was found to be suitable for the representation of all three wind velocity components. For neutral conditions, values of all three non-dimensional velocity variances were found to be smaller at the lowest measurement level and larger at higher levels in comparison to classical values found over flat terrain. Influence of surface heterogeneity was reflected in the ratio of observed dimensionless standard deviation of the vertical wind component and corresponding values of commonly used similarity formulas for flat and homogeneous terrain showing considerable variation with wind direction. The roughness sublayer influenced wind variances, and consequently the turbulent kinetic energy and correlation coefficients at the lowest measurement level, but not the wind shear profile. The observations support the classical linear expressions for the dimensionless wind shear (ϕ_m) even over inhomogeneous terrain after removing data points associated with the flux Richardson number (R_f) greater than 0.25. Leveling-off of ϕ_m at higher stabilities was found to be a result of the large number of data characterized by small-scale turbulence ($R_f > 0.25$). Deviations from linear expressions were shown to be mainly due to this small-scale turbulence rather than due to the surface heterogeneities, supporting the universality of this relationship. Additionally, the flux-gradient dependence on stability did not show different behavior for different wind regimes, indicating that the stability parameter is sufficient predictor for flux-gradient relationship. Data followed local z -less scaling for ϕ_m when the prerequisite $R_f \leq 0.25$ was imposed.

Key words: Stable boundary layer, Local scaling, Forest canopy, Roughness sublayer, Turbulent kinetic energy

Corresponding author at: Department of Geophysics, Faculty of Science, University of Zagreb,

Horvatovac 95, 10000 Zagreb, Croatia. Tel: +385 1 460 59 26.

E-mail address: babick@gfz.hr (K. Babić)

©2016. This manuscript version is made available under the CC-BY-NC-ND 4.0 licence

<http://creativecommons.org/licenses/by-nc-nd/4.0/>

32 1. Introduction

33 Stable atmospheric boundary layers (SBLs) are influenced by many independent forcings, such as,
34 (sub)mesoscale motions, which act on a variety of time and space scales, net radiative cooling, temperature
35 advection, surface roughness and surface heterogeneity (Mahrt, 2014) enhancing the complexities and
36 posing challenges in the study of the SBL. The fate of pollutants in the boundary layer is strongly affected
37 by turbulence which is extremely complicated in complex terrain and over heterogeneous surfaces.
38 Moreover, due to weak turbulence the SBL is generally favorable for the establishment of air pollution
39 episodes. Atmospheric dispersion models, used for air quality studies, as well as high-resolution regional
40 models use similarity scaling to model flow characteristics and dispersion in such environments.

41 Monin-Obukhov similarity theory (MOST) (Monin and Obukhov, 1954; Obukhov, 1946) relates surface
42 turbulent fluxes to vertical gradients, variances and scaling parameters. The assumptions underlying MOST
43 include stationary atmospheric turbulence, surface homogeneity and the existence of an inertial sublayer
44 (that is, surface layer, SL). Relations between these parameters (Businger et al., 1971; Dyer, 1974) are based
45 on several experimental campaigns conducted over horizontally homogeneous and flat (HHF) surfaces
46 (Kaimal and Wyngaard, 1990), where the original assumptions are considered to be met. Originally, MOST
47 was based on surface fluxes, which were assumed to be constant with height, and equal to surface values
48 within the SL (also referred to as constant-flux layer). In the unstable boundary layer, MOST has been
49 extensively studied and proven useful in relating turbulent fluxes to profiles (Businger et al., 1971; Dyer,
50 1974; Wyngaard and Coté, 1972). However, the applicability of MOST in the stable SL (e.g. Cheng et al.,
51 2005; Trini Castelli and Falabino, 2013) and over complex (Babić et al., 2016; Nadeau et al., 2013; Stiperski
52 and Rotach, 2016) and heterogeneous surfaces is still an open issue due to many difficulties when applying
53 traditional scaling rules since MOST assumptions may not be fulfilled. Nieuwstadt (1984) extended Monin-
54 Obukhov similarity in terms of a local scaling approach. This regime represents the extension of MOST
55 above the SL. Accordingly, all MOST variables are based on the local fluxes at a certain height z instead of
56 using surface values. As MOST should be valid over flat and homogeneous terrain, studies of the SBL in
57 terms of surface layer and local scaling approaches were made over areas characterized by long and uniform
58 fetch conditions, such as, Greenland, Arctic pack ice and Antarctica (Forrer and Rotach, 1997; Grachev et
59 al., 2013, 2007; Sanz Rodrigo and Anderson, 2013). Forrer and Rotach (1997) concluded that local scaling is
60 superior over surface layer scaling. This was mainly due to the fact that surface layer over an ice sheet, with

61 continuously stable stratification, can be very shallow (< 10 m). Moreover, for cases of strong stability, non-
62 dimensional similarity functions for momentum and heat were in agreement with the results obtained from
63 the local scaling approach. Grachev et al. (2013) examined limits of applicability of local similarity theory in
64 the SBL by revisiting the concept of a critical Richardson number.

65 Even modest surface heterogeneity can significantly influence the nocturnal boundary layer (NBL) and
66 lead to turbulence at higher Richardson numbers in comparison with homogeneous surfaces (Derbyshire,
67 1995). Since the earth's solid surfaces are mainly heterogeneous (at least to a certain degree), the interest in
68 flow and turbulence characteristics over complex surfaces has increased in recent decades. Moreover, a
69 proper representation of turbulence is particularly important for parameterization of surface-atmosphere
70 exchange processes in atmospheric models (e.g., dispersion, numerical weather prediction or regional
71 models). The turbulence characteristics have been studied through direct measurements for different
72 complex surfaces including, complex forest sites (e.g. Dellwik and Jensen, 2005; Nakamura and Mahrt,
73 2001; Rannik, 1998), agricultural fields, such as, apple orchard (e.g. de Franceschi et al., 2009) or rice
74 plantation (e.g. Moraes et al., 2005), metre-scale inhomogeneity (Andreas et al., 1998a), urban areas (e.g.
75 Fortuniak et al., 2013; Wood et al., 2010), and complex mountainous terrains (e.g. Rotach et al., 2008),
76 addressing to both valley floors (e.g. de Franceschi et al., 2009; Moraes et al., 2005; Rotach et al., 2004) and
77 steep slopes (Nadeau et al., 2013; Stiperski and Rotach, 2016). However, most of these studies are
78 associated with flows over homogeneous surfaces. In recent years much effort has been put into simulations
79 of turbulent fluxes over relatively heterogeneous surfaces using large-eddy simulations (LES, e.g. Calaf et
80 al., 2014). Bou-Zeid et al. (2007) used LES over surfaces with varying roughness lengths to assess the
81 parameterization for the equivalent surface roughness and the blending height in the neutral boundary layer
82 at regional scales. Large eddy simulations of surface heterogeneity effects on regional scale fluxes and
83 turbulent mixing in the stably stratified boundary layers were studied by Miller and Stoll, 2013; Mironov
84 and Sullivan, 2010; Stoll and Porté-Agel, 2008.

85 The vertical structure of the atmospheric boundary layer is traditionally partitioned into a SL, an outer
86 layer and the entrainment zone (e.g. Mahrt, 2000). The SL, in turn, is subdivided into a canopy layer (CL), a
87 roughness sublayer (RSL) and inertial sublayer. Over surfaces with small roughness elements the latter,
88 which corresponds to the true equilibrium layer, is often identified with SL. These concepts are less
89 applicable over heterogeneous surfaces but for the SBL they provide, nevertheless, a useful starting point.

90 Above very rough surfaces, such as forests or agricultural crops, the RSL has a non-negligible extension.
91 Due to the influence of individual roughness elements on the flow within the RSL (e.g. Finnigan, 2000;
92 Katul et al., 1999), MOST is not widely accepted. The existence of large-scale coherent turbulent structures
93 within the RSL, which are generated at the canopy top through an inviscid instability mechanism (Raupach
94 et al., 1996), is thought to be a reason for the failure of standard flux-gradient relationships (Harman and
95 Finnigan, 2010).

96 In the scientific community substantial effort was made to address MOST in different conditions. Most
97 of the observational studies are based on measurements from a single tower, and sometimes they result in
98 inconsistent conclusions on the applicability of similarity theory. These inconsistencies are mostly found for
99 studies of MOST in complex terrain (e.g. de Franceschi et al., 2009; Kral et al., 2014; Martins et al., 2009;
100 Nadeau et al., 2013) or for small scale turbulence for which z -less scaling regime should apply (e.g. Basu et
101 al., 2006; Cheng and Brutsaert, 2005; Forrer and Rotach, 1997; Grachev et al., 2013; Pahlow et al., 2001).
102 The main objective of the present paper is to examine the applicability of local similarity scaling over a
103 heterogeneous terrain influenced by a mixture of forest, agricultural and industrial surfaces, based on multi-
104 level turbulence observations in the wintertime SBL. Many of the above mentioned studies in complex
105 terrain are mainly characterized by homogeneous surface roughness, while studies over heterogeneous and
106 patchy vegetation are still scarce in the literature. Additionally, this paper relates to the approach of Grachev
107 et al. (2013), who investigated the limits of applicability of local similarity theory in the SBL over idealized
108 homogeneous surface of the Arctic pack ice. In the present work we use their approach to distinguish
109 between Kolmogorov and non-Kolmogorov turbulence, and consequently, to investigate whether classical
110 linear flux-gradient relationships can be applied for non-homogeneous surfaces. The paper is organized as
111 follows: in Section 2, we give a brief overview of the local scaling approach. In Section 3, we describe the
112 measurement site and measurements and we provide a description of post processing procedures. Section 4
113 contains our results for scaled standard deviations of wind components, turbulent kinetic energy, turbulent
114 exchange coefficients and non-dimensional wind profile. A summary and conclusions are given in Section 5.

115

116 **2. Local scaling**

117 Holtslag and Nieuwstadt (1986) presented an overview of scaling regimes for the SBL. Each of the
118 scaling regimes is characterized by different scaling parameters. The turbulence in the SL can be described

119 by MOST with surfaces fluxes of heat and momentum and the height z as scaling parameters. In this layer
 120 the relevant scaling parameter is the Obukhov length L (Obukhov, 1946), given by

$$L = -\frac{u_*^3}{k \frac{g}{\theta_v} (\overline{w'\theta'_v})_s} \quad (1)$$

121 where $u_* = (\overline{u'w'_s}^2 + \overline{v'w'_s}^2)^{1/4}$ is the surface friction velocity, $(\overline{w'\theta'_v})_s$ is the surface kinematic heat
 122 flux, $\overline{\theta_v}$ is the virtual potential temperature, g is the acceleration due to the gravity, $k=0.4$ is the von Kármán
 123 constant. Overbars and primes denote time averaging and fluctuating quantities, respectively.

124 Above the SL, the local scaling regime applies, a regime proposed by Nieuwstadt (1984). According to
 125 Nieuwstadt's local similarity approach, properly scaled turbulence statistics should solely be a function of the
 126 local stability parameter $\zeta_l = (z - d)/\Lambda$, where z is the measurement height, d is zero-plane displacement
 127 height and Λ is the local Obukhov length. Even if Nieuwstadt (1984) was not referring to rough surfaces, we
 128 have introduced d as we will be concerned with data from a site where the canopy height is non-negligible.
 129 In the local scaling framework, the local Obukhov length is based on the local fluxes at height z and varies
 130 with height

$$\Lambda = -\frac{u_{*l}^3}{k \frac{g}{\theta_v} \overline{w'\theta'_v}} \quad (2)$$

131 where u_{*l} indicates local friction velocity and $\overline{w'\theta'_v}$ is the local heat flux. Holtslag and Nieuwstadt (1986,
 132 their Fig. 2) showed that in the part of the SBL which encompasses a layer between 10 and 50 % of the total
 133 BL height at neutral stability and is exponentially decreasing with increasing stability, $\Lambda \approx L$. This indicates
 134 that the use of $(z-d)/\Lambda$, which is required by local scaling, is almost equivalent to the SL scaling parameter $(z-$
 135 $d)/L$. Therefore, the local scaling approach can be viewed as an extension of MOST for the entire SBL.

136 For large values of z/Λ ($z/\Lambda \rightarrow \infty$), the dependence on z disappears because stable stratification restricts
 137 vertical motion causing turbulence scales to be very small. Wyngaard and Coté (1972) named this limit
 138 "local z-less stratification" (height-independent). Based on the observations from a tall tower (Cabauw),
 139 Nieuwstadt (1984) found this limit to be for $\zeta_l > 1$.

140 Evaluation of second-order moments, especially of wind velocity standard deviations provides a good
 141 understanding of turbulence statistics. According to similarity theory, dimensionless quantities should be
 142 universal functions of the non-dimensional stability parameter. In the local scaling framework, standard

143 deviations of wind speed components σ_i , where $i = (u, v, w)$ denotes longitudinal, lateral and vertical
 144 velocity components, respectively, are scaled as

$$\phi_i = \frac{\sigma_i}{u_{*l}} \quad (3)$$

145 where ϕ_i represents a set of universal similarity functions, different for each velocity component. In the
 146 literature different formulations of the ϕ_i functions can be found. de Franceschi et al. (2009) presented a
 147 comprehensive review of various formulations of ϕ_i functions suggested by different studies and for
 148 different stabilities. A generally accepted form of the flux-variance similarity relationships in the stable
 149 boundary layer is

$$\phi_i(\zeta_l) = a_i(1 + b_i\zeta_l)^{c_i} \quad (4)$$

150 where coefficients a_i , b_i and c_i need to be found experimentally. Accordingly, the non-dimensional wind
 151 shear defined as

$$\phi_m(\zeta_l) = \frac{k(z-d)}{u_{*l}} \frac{\partial U}{\partial z} \quad (5)$$

152 where U is the mean wind speed, is also a unique function of stability. For neutral conditions ($\zeta = 0$), ϕ_m
 153 approaches unity. As the exact forms of the similarity functions are not predicted by similarity theory and
 154 they should be determined from field experiments, many different formulations have been proposed based
 155 on the data from different experiments (e.g. Beljaars and Holtslag, 1991; Cheng and Brutsaert, 2005; Dyer,
 156 1974; Grachev et al., 2007; Sorbjan and Grachev, 2010). We will compare our results to the linear
 157 relationship of Dyer (1974) obtained for the stable SL

$$\phi_m(z/L) = 1 + b_m \frac{z}{L} \quad (6)$$

158 where $b_m = 5$. Högström (1988) modified several existing formulas for ϕ_m (and also for the non-
 159 dimensional temperature profile, ϕ_h), in order to comply with his assumptions of $k = 0.4$ and $(\phi_h)_{\zeta=0} =$
 160 0.95 . For Dyer's expression (6), he obtained a value $b_m = 4.8$. Additionally, we compare our results to the
 161 non-linear stability function of Beljaars and Holtslag (1991)

$$\phi_m(z/L) = 1 + a \frac{z}{L} + b \frac{z}{L} e^{-d \frac{z}{L}} - bd \frac{z}{L} \left(\frac{z}{L} - \frac{c}{d} \right) e^{-d \frac{z}{L}} \quad (7)$$

162 where $a = 1$, $b = 0.667$, $c = 5$, $d = 0.35$, as expressions (6) and (7) are probably the most often used for
 163 parameterization in numerical models. Both relationships were derived over flat and homogeneous terrain
 164 using Obukhov length, which is based on surface values. While the first expression was derived and verified

165 by different experiments in the stability range $0 < z/L < 1$, Eq. (7) is valid in strongly stable conditions were
 166 the overestimation of the non-dimensional gradients is reduced. Linear equations for the stable SL together
 167 with the relations for the unstable conditions are traditionally called Businger-Dyer relations (Businger et al.,
 168 1971; Dyer, 1974). Similar to the non-dimensional velocity variances we use the non-dimensional wind
 169 shear in its local form (see Eq. (5)).

170 Another widely used stability parameter is the flux Richardson number, defined based on the vertical
 171 gradient of wind speed

$$Rf = \frac{-\frac{g}{\theta_v} \overline{w'\theta'_v}}{u_*^2 \frac{\partial U}{\partial z}}. \quad (8)$$

172 Grachev et al. (2013) argued that the upper limit for applicability of the local similarity theory is determined
 173 by the inequalities $Ri < Ri_{cr}$ and $Rf < Rf_{cr}$, where Ri is the gradient Richardson number. They found both
 174 critical values to be equal to $Ri_{cr} = Rf_{cr} = 0.20 - 0.25$, with $Rf_{cr} = 0.20 - 0.25$ being the primary
 175 threshold. The z -less concept requires that z cancels in Eqs. (4) and (6). As a result, a linear relationship for
 176 the non-dimensional function ϕ_m is obtained, while non-dimensional functions ϕ_i asymptotically approach
 177 constant values:

$$\phi_m(\zeta_l) = b_m \zeta_l, \quad (9)$$

$$\phi_i = b_i, \quad (10)$$

178 where b_m and b_i are experimentally determined coefficients. For convenience, throughout this paper we will
 179 use the notation $\zeta = \zeta_l$ as all variables are based on local values.

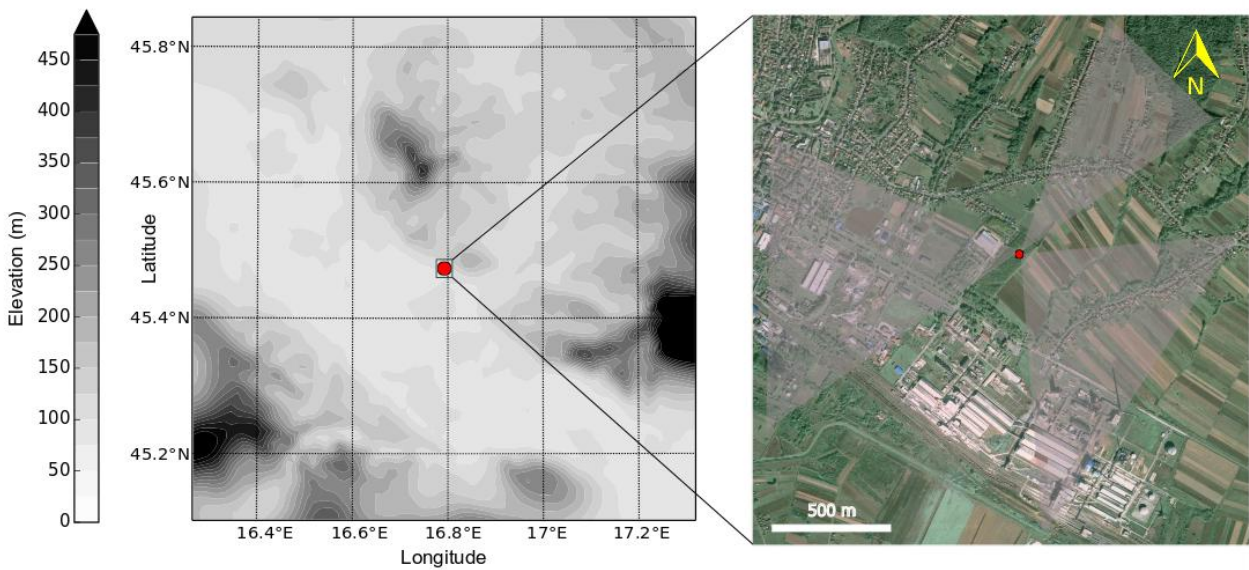
180

181 3. Data and Methods

182 3.1. Site description

183 A 62 m high tower was located in the vicinity of the small industrial town Kutina, Croatia (tower
 184 coordinates: 45°28'32"N, 16°47'44"E). The tower was placed above a grassy surface and it was surrounded
 185 by approximately 18 m high black walnut (*Juglans nigra*) trees. The closest trees are approximately 20–25
 186 m away from the tower and they encompass an area of approximately 120–480 m² (Fig. 1). The tower is
 187 situated in a rather heterogeneous surrounding regarding both a larger spatial scale (Fig. 1a) and immediate
 188 vicinity of the measurement site (on the order of 1 km distance, Fig. 1b). To the east of the tower, crop

189 fields, which extend to the aerial distance of more than 1 km, are found. South-southeast of the tower, about
 190 800 m to 1.5 km distant a large petrochemical industry plant is placed. In a sector that encounters winds
 191 from the north-northwest to the northeast, low, forested hills are located. They are covered with a dense
 192 forest, while at lower elevations, cultivated orchards and vineyards are found. Fooths of these hills are
 193 roughly 1.3 km away from the measurement site. Thus, due to different surface roughness features
 194 measurements in the SBL at the measuring site may be contaminated by local advective fluxes, drainage
 195 flows and/or orographically-generated gravity waves. These features are related to (sub)mesoscale motions
 196 which do not obey similarity scaling and are therefore removed from our data by the rigorous data quality
 197 control and post-processing options as described later in the paper (Section 3.2.). We are thus focusing on
 198 the micrometeorologically complex local site characteristics, which may be more typical for real sites than
 199 the usually investigated homogeneous reference sites.



200
 201 **Fig. 1.** (a) Topographic map with contour lines each 25 m of the area surrounding the measurement site (red
 202 dot) representing inhomogeneous terrain on a larger spatial scale. (b) Google Maps image (Image © 2015
 203 DigitalGlobe) of the observational site. Measurement tower is indicated with a red dot (45°28'32"N,
 204 16°47'44"E). Light gray shaded areas correspond to wind directions depicted in Fig. 5.

205
 206 Data used in this study were collected during wintertime (1 December 2008–28 February 2009) and
 207 correspond to the nocturnal period from 1800 to 0600 local time. Turbulence measurements of three-
 208 dimensional wind and sonic temperature were continuously measured using identical WindMaster Pro (Gill
 209 Instruments) ultrasonic anemometers that sampled at 20 Hz. Data were measured at five levels above the

210 canopy height, hereafter at level 1 ($z_1 = 20$ m above the surface), level 2 ($z_2 = 32$ m), level 3 ($z_3 = 40$ m),
 211 level 4 ($z_4 = 55$ m) and level 5 ($z_5 = 62$ m). Measurement levels were prescribed prior to the experiment
 212 through existing tower infrastructure. Given the complicated and spatially inhomogeneous characteristics of
 213 the measurement site, an idealized vertical structure is considered as a zero-order approach in the analysis.
 214 Estimate of vertical layers for neutral conditions was done using different models available in the literature
 215 and serves as a simple model for the interpretation of the results. For stably stratified conditions these
 216 estimates will not be perfectly appropriate, but will provide the gross picture.

217 Conceptually, when the air flows over changing terrain, the downwind surface conditions are likely to
 218 influence the measurements via internal boundary layers (IBLs), which grow in height (h_i) with downwind
 219 distance (Fig. 2) (e.g. Cheng and Castro, 2002; Dellwik and Jensen, 2005). Only the lowest portion of the
 220 IBL (10%) is in equilibrium with the new surface (internal equilibrium layer, IEL) while the flow above the
 221 IBL is in equilibrium with the upstream surface conditions. The IEL can, finally, be identified with the
 222 inertial sublayer (IS). However, if the new surface is very rough its lower part must be considered as a RSL.
 223 Within the upper part of the IEL, i.e. IS, turbulent fluxes are approximately constant with height, MOST is
 224 valid and the mean wind speed follows the expected logarithmic profile. Within the RSL, the flow is
 225 influenced by the distribution and structure of canopy elements (Monteith and Unsworth, 1990; Rotach and
 226 Calanca, 2014), with momentum and scalars transported by turbulence, wake effects and molecular diffusion
 227 (Malhi, 1996). Above the height of the IEL (h_e) stress and fluxes start to decrease due to the upwind
 228 influence. This layer is defined as a transition layer (Fig. 2). Due to the very tall roughness elements we use
 229 the zero-plane displacement height (d) as our reference - hence the IBL is assumed to range from $z = d$ up
 230 to $z = h_i + d$. Ideally, after a long enough flow over the new surface the IBL fills the entire boundary layer.
 231 Since we are interested in evaluating the degree to which local scaling applies under inhomogeneous fetch
 232 conditions we map the idealized SBL structure to the IBL. The transition layer then becomes the outer part
 233 of the inhomogeneously forced SBL.

234 We have estimated the length scales introduced above as follows: h_i is estimated based on the model of
 235 Cheng and Castro (2002)

$$\frac{h_i}{z_{02}} = 10.56 \left(\frac{x}{z_{02}} \right)^{0.33}, \quad (11)$$

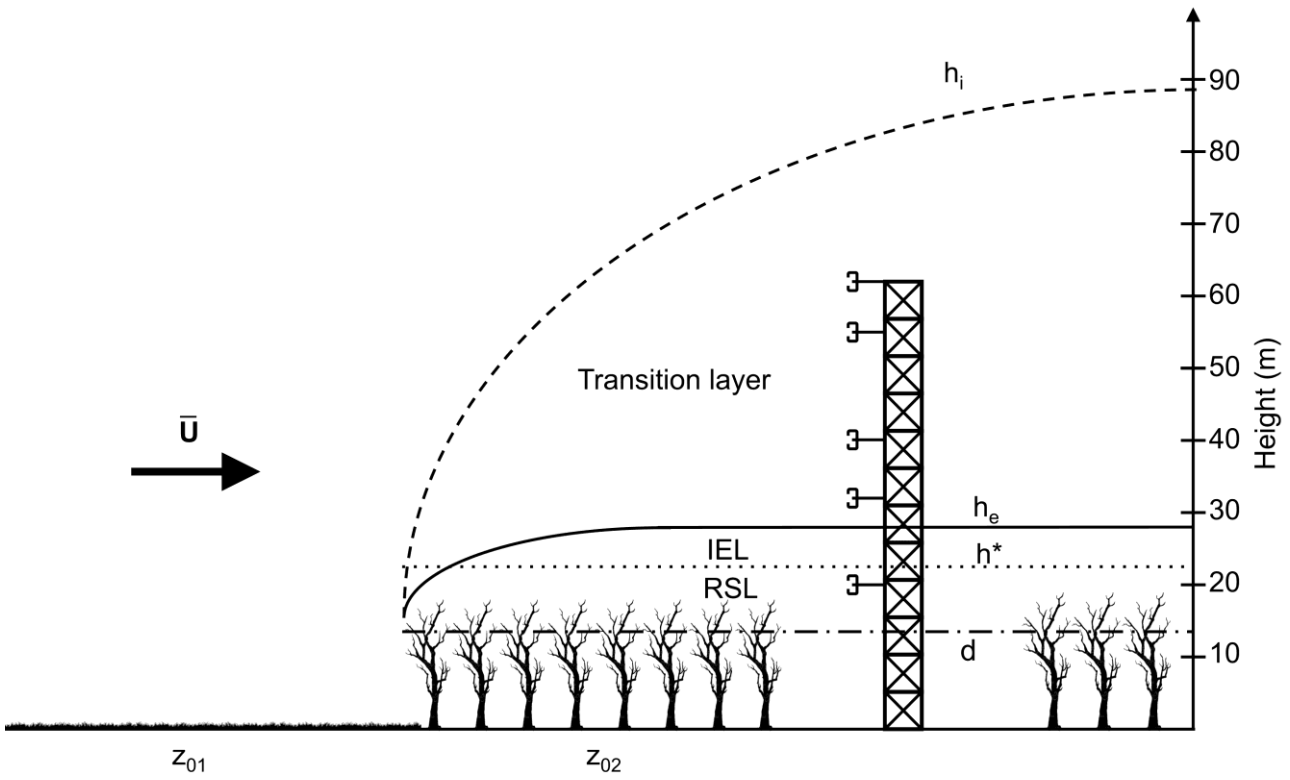


Fig. 2. Conceptual sketch of idealized vertical layers after a step change in surface roughness for the long fetch case (391 m) under neutral conditions. The height of the IBL (h_i), which develops due to the change in roughness conditions, is estimated based on the model of Cheng and Castro (2002). Above the h_i the flow is in equilibrium with the upwind surface. Within the internal equilibrium layer (IEL) the flow is in equilibrium with the forest. The transition layer indicates the transition zone between upwind and downwind equilibrium conditions. The dotted line denotes the height of the RSL, h^* , estimated based on relation of Raupach (1994). The dash-dot line shows the zero-plane displacement height (d) estimated as $3/4h_c$ (Kaimal and Finnigan, 1994; Stull, 1988). z_{01} and z_{02} correspond to upwind and downwind roughness lengths, respectively. The black arrow denotes the mean wind (U) direction.

where x is the distance to the roughness change from the position of measurement (fetch) and z_{02} is the roughness length of the new surface. Following Cheng and Castro (2002), h_e can be determined as

$$\frac{h_e}{z_{02}} = 1.47 \left(\frac{x}{z_{02}} \right)^{0.37}. \quad (12)$$

The depth of the RSL (h^*) depends on different properties, such as canopy density, roughness length for momentum and tree height. Raupach (1994) estimated the height of the RSL as

$$\frac{h^* - d}{h_c - d} = 2. \quad (13)$$

For the zero-plane displacement we use a straightforward methodology, $d = \frac{3}{4}h_c$ (Kaimal and Finnigan, 1994; Stull, 1988), where $h_c = 18$ m is the average canopy height, which is estimated through direct

253 measurements (using laser distance meter). Additionally, for the walnut forest we used $z_{02} = 1$ m (the lower
 254 value for the roughness length over forest, $z_0 = 1$ m, according to Foken (2008), his Table 3.1).

255 The estimated height of the IBL at our site (Tab. 1) varied between 40 and 76 m for short (≈ 56 m) and
 256 long (≈ 390 m) fetch conditions, respectively. Estimated values of h_e at the location of the tower ranged
 257 between 6.5 and 13.7 m according to Cheng and Castro (2002) for short and long fetch cases, respectively.

258

259 **Table 1**

260 Height of the equilibrium layer (h_e) and of the internal boundary layer (h_i) estimated based on the model of
 261 the Cheng and Castro (2002) (Eqs. (11) and (12)) for different fetch (x) values corresponding to particular
 262 wind directions (WD). Note that these heights indicate the height above the displacement height d . In the
 263 determination of the fetch length, holes in the forest or corridors of vegetation other than forest were
 264 disregarded if their size was small enough.

WD (deg)	30	60	90	120	150	180	210	240	270	300	330	360
x (m)	92	89	69	56	58	77	391	415	110	84	78	105
h_e (m)	7.8	7.7	7.0	6.5	6.6	7.3	13.4	13.7	8.3	7.6	7.4	8.2
h_i (m)	47	46	43	40	40	44	76	77	50	46	44	49

265

266 These estimates indicate that the second measurement level is above the IEL height ($z = h_i + d$) for all
 267 wind directions. Also, the height of the RSL at our measurement site is $h^* = 1.25h_c$, that is, approximately
 268 22.5 m. Using the above estimates, we find that level 1 is likely to be within the RSL for all wind directions.
 269 For cases characterized with the short fetch, the IEL will most likely be within the RSL ($h_e + d < h^*$),
 270 while only for wind direction with large fetch conditions (200–250 deg) the growing equilibrium layer will
 271 encompass the RSL and a thin IS will form. Levels 2 and 3 are in the transition layer for all wind directions,
 272 while levels 4 and 5 are even above h_i for the short fetches (105–175 deg). The highest measurement level
 273 reflects the upwind surface conditions for fetches shorter than 100 m. Hence a potential RSL influence
 274 should be detectable if level 1 behaves differently. If levels 2–5 do not show different behavior this can be
 275 taken as an indication that our crude mapping assumption has some validity.

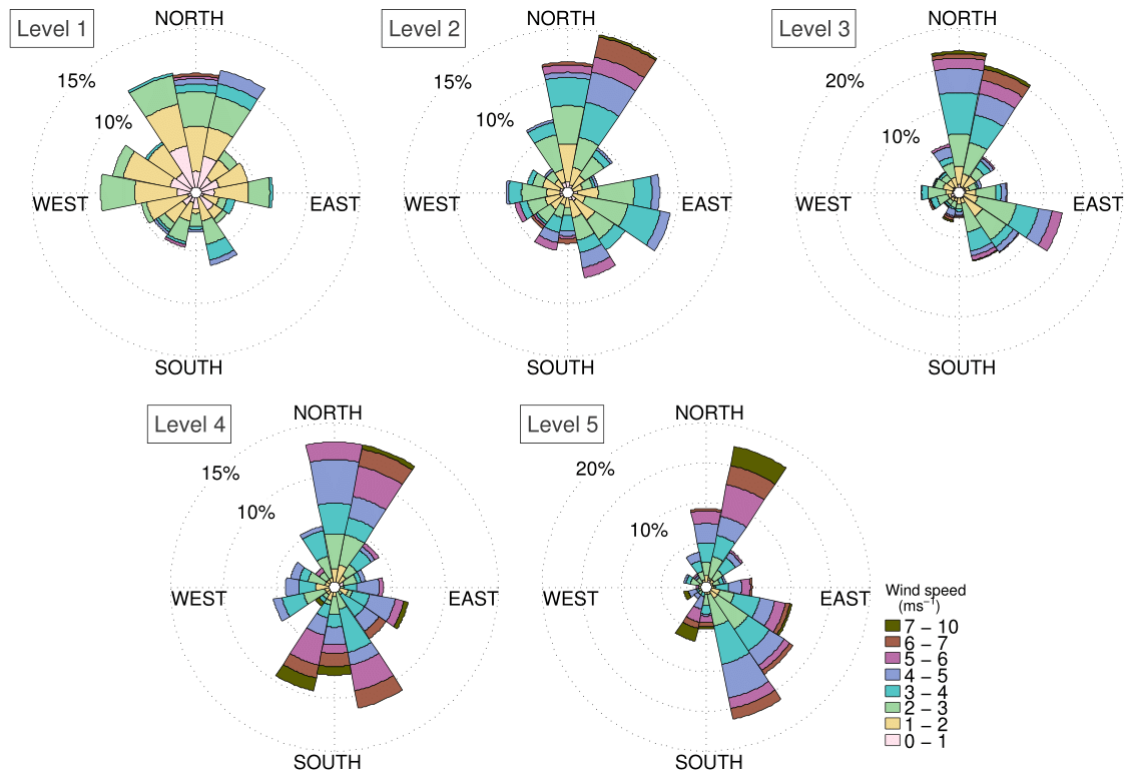
276

277 3.2. Post processing of the data

278 Instruments were mounted 3 m away from the triangular lattice tower (booms facing to the northeast) to
 279 minimize any flow distortion effect by the tower. Considerable loss of data was incurred due to intermittent

280 winter icing or temporary instrument malfunction (Table 2). During this period, light nocturnal winds were
281 common at the site at the lowest measurement level (Fig. 3). We assume that the sonic temperature $T_s =$
282 $T(1 + 0.51q)$, where T is the air temperature, is close to the virtual potential temperature θ_v . Automated
283 quality control procedures were not used since they may be too strict for the SBL analysis of weak
284 turbulence. Raw 20-Hz data were first divided into 30-min intervals. These intervals were checked for large
285 data gaps, and all 30-min intervals with more than 1% of missing data were omitted from further analyses.
286 After the consistency limits check, where we removed the data having unrealistically high values, spikes
287 (defined as data points within the time series which deviate more than four standard deviations from the
288 median value of the particular 30-min averaging window) were removed. If the number of spikes within the
289 30-min interval was less than 1% of the total data, spikes were replaced by linear interpolation from
290 neighboring values. We calculated angles of attack for each measurement and for each flux averaging
291 period, and flagged it if angles of attack exceeded 15 deg. The number of 30-min intervals available for the
292 further post-processing is labeled as “minimum QC” (Table 2). A cross-correlation correction of the time
293 series is already implemented in the Gill Instruments software.

294 Although double rotation of the data is the most commonly used to correct for sonic misalignment,
295 according to Mahrt (2011) and Mahrt et al. (2013) it should not be applied to SBL data under weak-wind
296 conditions. In the very stable boundary layer direction-dependent mean vertical motions may occur where
297 minor surface obstacles can significantly perturb the flow. In a setup like ours characterized by tall
298 vegetation and/or complex terrain, a non-zero 30-min mean vertical wind component may exist. In such
299 situations a planar fit (PF) method (Wilczak et al., 2001) would be better since it is based on an assumption
300 that the vertical wind component is equal to zero only over longer averaging periods. PF method performs a
301 multiple linear regression on the 30-min wind components to obtain the mean streamline plane (Aubinet et
302 al., 2012). This plane is based on the measurements made during the 88-night period for each of five levels
303 (Table 2).



304

305 **Fig. 3.** Wind roses at the measurement site for 30-min averaged data for the analyzed period (December
 306 2008–February 2009). Levels 1 to 5 correspond to measurement heights of 20, 32, 40, 55 and 62 m above
 307 the ground, respectively.

308

309 Basu et al. (2006) have shown that using an averaging window of inappropriate length can lead to false
 310 conclusions concerning the behavior of the turbulence. In stable flows, use of an averaging time that is too
 311 large leads to serious contamination of the computed flux by incidentally captured mesoscale motions
 312 (Howell and Sun, 1999; Vickers and Mahrt, 2003). Previously Babić et al. (2012) applied two methods
 313 based on Fourier analysis to determine an appropriate turbulence averaging time scale. In this study, we have
 314 used a multiresolution flux decomposition (MFD) method (Howell and Mahrt, 1997) as described in Vickers
 315 and Mahrt (2003). If the gap timescale is employed in the calculation of turbulent fluctuations,
 316 contamination by mesoscale motions should be removed. Accordingly, in comparison with the use of an
 317 arbitrary averaging time scale, similarity relationships should be improved. Here, based on the MFD method
 318 we obtained a gap timescale of 100 sec, which is shorter than the previous value obtained by Babić et al.
 319 (2012) for a single night case. Thus, a value of 100 sec was used here for a high-pass filtering of the time
 320 series of raw u , v , w and T_s by applying a moving average. Since averaging over a longer time period (i.e. 30
 321 or 60 min) reduces random flux errors in the case of relatively stationary turbulence, turbulent variances and

322 covariances in the present study correspond to 30-min averages. The mean wind speed and wind direction
323 were derived from the sonic anemometer data.

324 Stationarity of the time series is a fundamental assumption of similarity theory. Thus, it should be tested
325 prior to evaluation of similarity theory. Večenaj and De Wekker (2015) performed a comprehensive analysis
326 to detect non-stationarity based on various tests proposed in the literature. They found that the Foken and
327 Wichura (1996) test most often detects the largest number of non-stationary time intervals among all the
328 tests investigated. They concluded that non-stationarity significantly decreases if detrending or high-pass
329 filtering is applied, since highly non-stationary (sub)mesoscale motions are removed by filtering.
330 Therefore, while testing non-stationarity of our datasets we first removed the linear trend for each 30-min
331 interval and then applied the Foken and Wichura (1996) test to the filtered time series. The percentage of
332 non-stationary periods for our dataset over heterogeneous terrain in the SBL varied between 20 and 30 %
333 depending on the level of observation (Table 2). This is slightly lower compared to studies of complex
334 mountainous terrain of Večenaj and De Wekker (2015) and Stiperski and Rotach (2016).

335 The statistical uncertainty (or sampling error) is inherent to every turbulence measurement. The
336 assessment of the statistical uncertainty is related to the averaging period. In order to estimate statistical
337 uncertainty we followed Stiperski and Rotach (2016). We performed this test on the time intervals which
338 were declared stationary by the foregoing test. The statistical uncertainty was estimated for the momentum
339 and heat fluxes, and for the variances. This was done for the fixed averaging period of 30-min. Although
340 over ideally flat and homogeneous surfaces one might choose 20% as a limit of statistical uncertainty, we
341 chose the 50% to assure both, high quality data sets, and a significantly large amount of input data for the
342 similarity analysis (Stiperski and Rotach, 2016). Thus, for the subsequent analysis only 30-min intervals
343 associated with statistical uncertainty below 50% were chosen. The uncertainty was largest for the kinematic
344 heat flux while for variances it was on average smaller than 50%.

345 Finally, following the QC recommendations by e.g. Klipp and Mahrt (2004) and Grachev et al. (2014)
346 we imposed the following thresholds: data with the local wind speed less than 0.2 ms^{-1} were omitted, while
347 minimum thresholds for the kinematic momentum flux, kinematic heat flux, and standard deviation of each
348 wind speed component were 0.001 ms^{-1} , 0.001 Kms^{-1} and 0.04 ms^{-1} , respectively.

349
350

351 **Table 2**

352 Number of 30-min intervals that satisfy the minimum QC (no large data gaps, no unrealistic values and no
 353 spikes) within the observed period of 88 nights (out of a total of 2112 possible intervals). The number of
 354 stationary and also the number of time intervals which are stationary and have uncertainty < 50% (used for
 355 the analysis in this study) is given.

Crtieria	Level 1	Level 2	Level 3	Level 4	Level 5
Minimum QC	647	802	1898	564	803
Stationary	482	576	1323	388	649
Stationary & Uncertainty < 50%	342	388	760	225	357

356
 357

358 Footprints are estimated and used in order to facilitate an interpretation of the results. Kljun et al. (2015)
 359 presented a new parameterization for Flux Footprint Prediction (FFP) which has improved footprint
 360 predictions for elevated measurement heights in stable stratification. Furthermore, the effect of the surface
 361 roughness has been implemented into the scaling approach. It is based on a scaling approach of flux
 362 footprint results of a thoroughly tested Lagrangian footprint model. A two-dimensional flux footprint model
 363 of Kljun et al. (2015) (<http://footprint.kljun.net/>) was used to estimate the surface upwind of the
 364 measurement tower that defined the fetch (flux footprint function) for the measurements at each level during
 365 stable conditions. As input parameters we used the mean standard deviations of lateral wind component (σ_v
 366 = 0.40, 0.45, 0.41, 0.46 and 0.46 ms⁻¹ for levels from 1 to 5, respectively), the mean local Obukhov lengths
 367 ($\Lambda = 33, 28, 38, 45$ and 39 m), the mean friction velocities ($u_{*l} = 0.23, 0.20, 0.19, 0.22$ and 0.21 ms⁻¹) and
 368 correspondingly, mean wind velocity for each measurement height ($U = 1.9, 2.9, 3.1, 4.0$ and 4.1 ms⁻¹). The
 369 height of the SBL was set to 250 m since the result did not exhibit noticeable sensitivity to its choice. The
 370 peak location of the footprint function, i.e. location of the maximum influence on the measurement,
 371 increases with increasing height and varies between 19 and 405 m from the lowest to the highest
 372 observational level, respectively. Additionally, the distance from the receptor that includes 90% of the area
 373 influencing the measurement (x_R) increases with height, where $x_R \approx 65, 331, 570, 1260$ and 1300 m,
 374 correspond to levels 1 to 5, respectively.

375

376 3.3. *Assesment of self-correlation*

377 Monin-Obukhov as well as local similarity theory leads to self-correlation, because both predicted
 378 variables and the predictors are functions of the same input quantities (Hicks, 1978). As an example,
 379 prediction of σ_i/u_{*l} ($i = u, v, w$) or ϕ_m in terms of the stability parameter contains self-correlation since both

380 σ_i/u_{*l} or ϕ_m and ζ depend on u_{*l} . To test the role of self-correlation in our dataset, we followed the
381 approach of Mahrt (2003) as described in Klipp and Mahrt (2004), using 1000 random samples. Random
382 datasets were created by redistributing the values of σ_u , σ_v , σ_w , u_{*l} and dU/dz from the original dataset for
383 each measurement level. We used threshold values $-\overline{w'\theta'_v} > 0.001 \text{ mKs}^{-1}$ and $dU/dz > 0.001 \text{ s}^{-1}$, as values
384 less than these are indistinguishable from zero. We repeated this process 1000 times and we calculated
385 corresponding 1000 random linear-correlation coefficients between σ_i and ζ and ϕ_m and ζ . The average of
386 these 1000 random correlation coefficients, $\langle R_{rand} \rangle$, is a measure of self-correlation because random data no
387 longer have any physical meaning. The difference between the squared correlation coefficient of the original
388 dataset R_{data}^2 and $\langle R_{rand}^2 \rangle$ is proposed as a measure of the actual fraction of variance attributed to the
389 physical process. A very small value of the linear-correlation coefficient (< 0.15) indicates no correlation
390 between compared variables. Mahrt (2014) stated that physical interpretation of results becomes ambiguous
391 when the self-correlation is of the same sign as the expected physical correlation. However, this test does not
392 seem to be appropriate for near-neutral and very stable cases (z -less limit), since σ_i/u_{*l} and ϕ_m tend to
393 constant values, resulting in small (or even negative) correlation coefficients (Babić et al., 2016)

394

395 **4. Results and Discussion**

396 *4.1. Flux-variance similarity*

397 Variances of wind velocity components provide important information on turbulence intensity as well as
398 for the modeling of turbulent kinetic energy and transport. In this section we evaluate similarity of scaled
399 standard deviations of wind velocity components. Normalized standard deviations of wind components are
400 plotted as a function of the local stability parameter in Figs. 4 and 6. Figure 4 shows that scatter of the data
401 (gray symbols) increases with increasing height, where standard deviations of 0.27, 0.29, 0.41, 0.36 and 0.34
402 ms^{-1} correspond to levels from 1 to 5, respectively. Note that the number of data is the largest at level 3.
403 Moreover, after applying strict quality control criteria the scatter is substantially reduced (standard
404 deviations in the range 0.21–0.23 ms^{-1}). This is similar to results of Babić et al. (2016), and opposed to some
405 other studies in complex terrain (e.g. Fortuniak et al., 2013; Nadeau et al., 2013; Wood et al., 2010).
406 Stationary data that exceed our uncertainty threshold of 50% are presented in order to show the influence of
407 small fluxes (which are difficult to measure and hence uncertain) on the scatter of σ_w/u_{*l} (presented as
408 gray symbols in Fig. 4). As seen from Fig. 4, this criterion is crucial for excluding the high values of the

409 scaled vertical wind variance in the strongly stable regime where z -less scaling should be valid. Without this
 410 exclusion, an incorrect conclusion on the validity of z -less scaling might be drawn. In the subsequent
 411 analysis these data are omitted and individual data as well as bin-averages in all figures correspond to data
 412 (namely, wind variances and turbulent fluxes) which satisfy an uncertainty limit $< 50\%$.

413 To evaluate the similarity of the scaled standard deviations we used the relationship form (4), where a_i ,
 414 b_i and c_i ($i = u, v, w$) are free fitting parameters (e.g. Wood et al., 2010). The best-fit coefficients were
 415 obtained using a robust least-squares fit of all 30-min data (Table 3). We note that values of fitting parameter
 416 a_i (neutral limit) for all three non-dimensional velocity variances are smallest at the lowest measurement
 417 level. Also, they are smaller than the canonical values for flat and uniform terrain ($\sigma_u/u_* = 2.39 \pm$
 418 $0.03, \sigma_v/u_* = 1.92 \pm 0.05, \sigma_w/u_* = 1.25 \pm 0.03$, Panofsky and Dutton (1984)) which clearly indicates
 419 influence of the RSL. This justifies our estimates of the vertical structure and footprints. Turbulence
 420 characteristics and transport in this layer are determined by the presence of coherent structures which are
 421 generated at the canopy top (e.g. Finnigan and Shaw, 2000; Shaw et al., 2006). These coherent eddies and
 422 extra mixing are generated by the inviscid instability mechanism (Raupach et al., 1996). Values of $a_{v,w}$ at
 423 levels 2–5 are larger compared to the Panofsky and Dutton (1984) values for the neutral range, while the a_u
 424 value for level 2 is larger. For three other levels values are slightly smaller (Table 3). Values of σ_w/u_{*l}
 425 larger than 1.25 (value reported for “ideal” flat terrain) are often observed over non-uniform terrain and may
 426 be attributed to horizontal momentum transport (Katul et al., 1995).

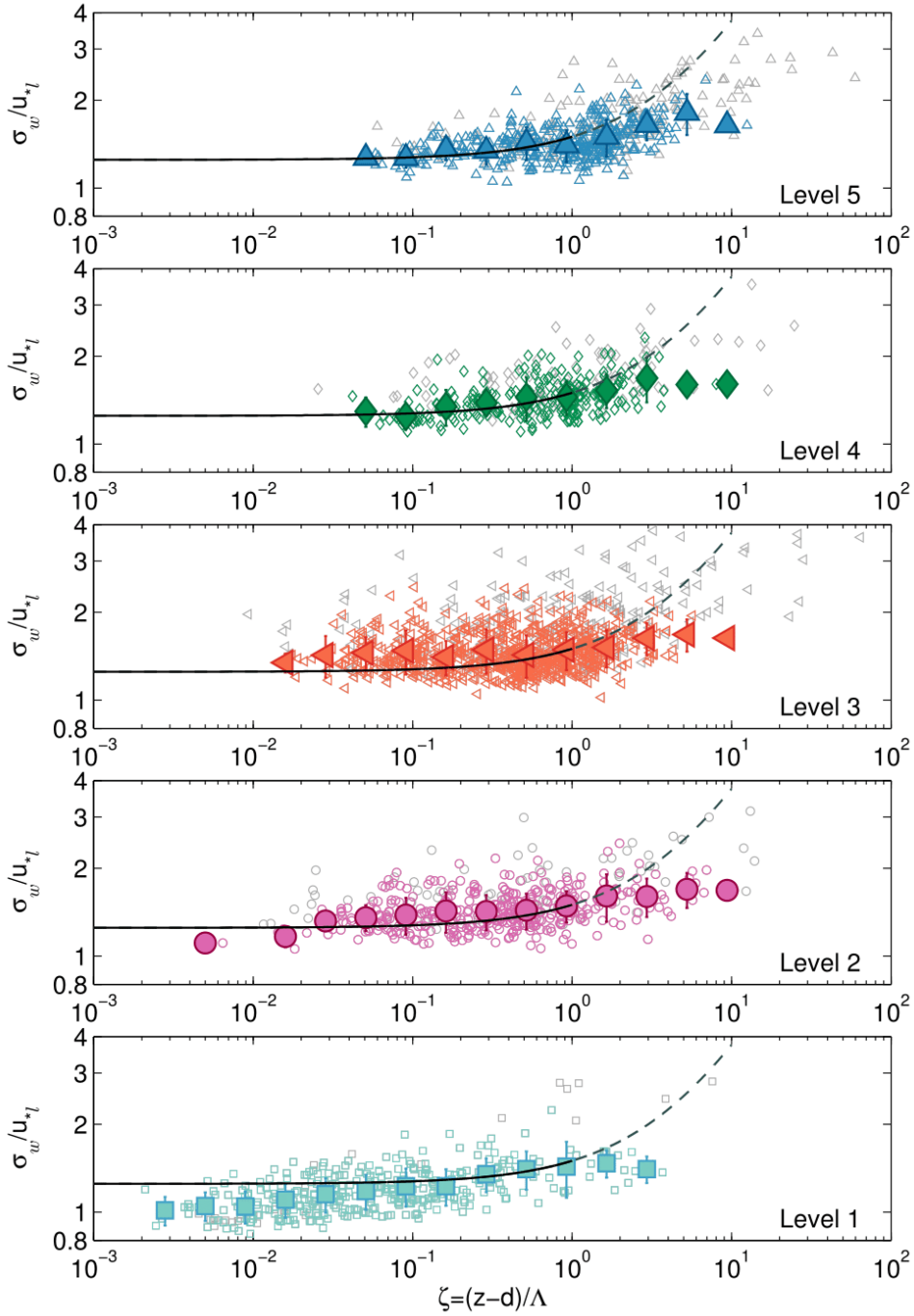
427

428 **Table 3**

429 Fitted relationships for non-dimensional standard deviations of wind components. Functional forms (Eq. (4))
 430 of non-dimensional standard deviations of velocity components were tested using a robust least-squares
 431 method.

Level	Height*	σ_u/u_{*l}	σ_v/u_{*l}	σ_w/u_{*l}
Level 1	20 m	$2.10(1 + 7.27\zeta)^{0.09}$	$1.30(1 + 1506\zeta)^{0.1}$	$0.94(1 + 656\zeta)^{0.06}$
Level 2	32 m	$2.48(1 + 0.57\zeta)^{0.12}$	$2.10(1 + 9\zeta)^{0.1}$	$1.34(1 + 3.39\zeta)^{0.08}$
Level 3	40 m	$2.32(1 + 0.15\zeta)^{0.36}$	$2.00(1 + 1.9\zeta)^{0.1}$	$1.43(1 + 0.18\zeta)^{0.26}$
Level 4	55 m	$2.24(1 + 0.79\zeta)^{0.15}$	$1.70(1 + 6.7\zeta)^{0.1}$	$1.21(1 + 15.94\zeta)^{0.07}$
Level 5	62 m	$2.13(1 + 0.75\zeta)^{0.17}$	$2.00(1 + 0.9\zeta)^{0.2}$	$1.30(1 + 0.59\zeta)^{0.22}$

432 * above ground level



433

434 **Fig. 4.** Scaled standard deviation of vertical velocity fluctuations as a function of stability. Black solid line
 435 ($0 < \zeta < 1$) corresponds to: $\phi_w = 1.25(1 + 0.2\zeta)$ (Kaimal and Finnigan, 1994). Thin dashed line is an
 436 extension for $1 < \zeta < 10$. Individual data at each level are shown as background symbols (gray symbols
 437 represent stationary data points which exceed our uncertainty threshold of 50%). Error bars indicate one
 438 standard deviation within each bin. The bin size is determined in a logarithmic scale using fifteen equally
 439 spaced bins in the stability range $0.002 < \zeta < 12.5$.

440

441 As already mentioned, flux-variance similarity relationships are influenced by self-correlation. Small
 442 values of fitted coefficients b_i and/or c_i indicate the best-fit curve which converges to a constant, i.e. a_i .
 443 Consequently, values of R_{data}^2 tend to converge to small values or even to zero, while $\langle R_{rand}^2 \rangle$ are usually
 444 larger which leads to negative values of $R_{data}^2 - \langle R_{rand}^2 \rangle$. The same result was obtained by Babić et al.
 445 (2016) and, as they pointed out, this presents a limitation of the method since it relies on the linear
 446 correlation coefficient and does not allow for a reliable conclusion about self-correlation in the SBL.

447 Table 4 presents a review of $\sigma_{u,v,w}/u_{*l}$ published in the literature for different terrain characteristics
 448 under neutral conditions. As already noted, dimensionless velocity variances in the RSL often exhibit
 449 lower values in comparison with the flat terrain reference of Kaimal and Finnigan (1994). Our results for
 450 $\sigma_{u,v}/u_{*l}$ at the lowest measurement level are in the range of values obtained within RSLs over forest
 451 (Rannik, 1998) and urban (Rotach, 1993) areas. For levels 2–5, neutral values are close to those reported
 452 by Moraes et al. (2005) and Wood et al. (2010). Using local scaling over the city of London
 453 (measurements at 190 m above the ground), Wood et al. (2010) obtained near-neutral limits of σ_i/u_{*l}
 454 ($i = u, v, w$), which are in accordance with those reported for flat and homogeneous terrain where MOST
 455 applies. They concluded that MOST was not complicated by too many factors, since London is quite flat
 456 and there are consistent building heights across a wide area which produced a longer upwind fetch causing
 457 the London boundary layer likely to be in equilibrium with the surface. Our results for σ_w/u_{*l} are
 458 furthermore consistent with Nieuwstadt (1984) who found it to be constant (~ 1.4) in the stability range
 459 $0.1 < \zeta < 2$.

460 **Table 4**

461 Comparison of neutral values for non-dimensional standard deviations of the wind from different studies.
 462 Our near-neutral values correspond to the mean value of scaled standard deviations of wind in the range
 463 $0 < \zeta < 0.05$.

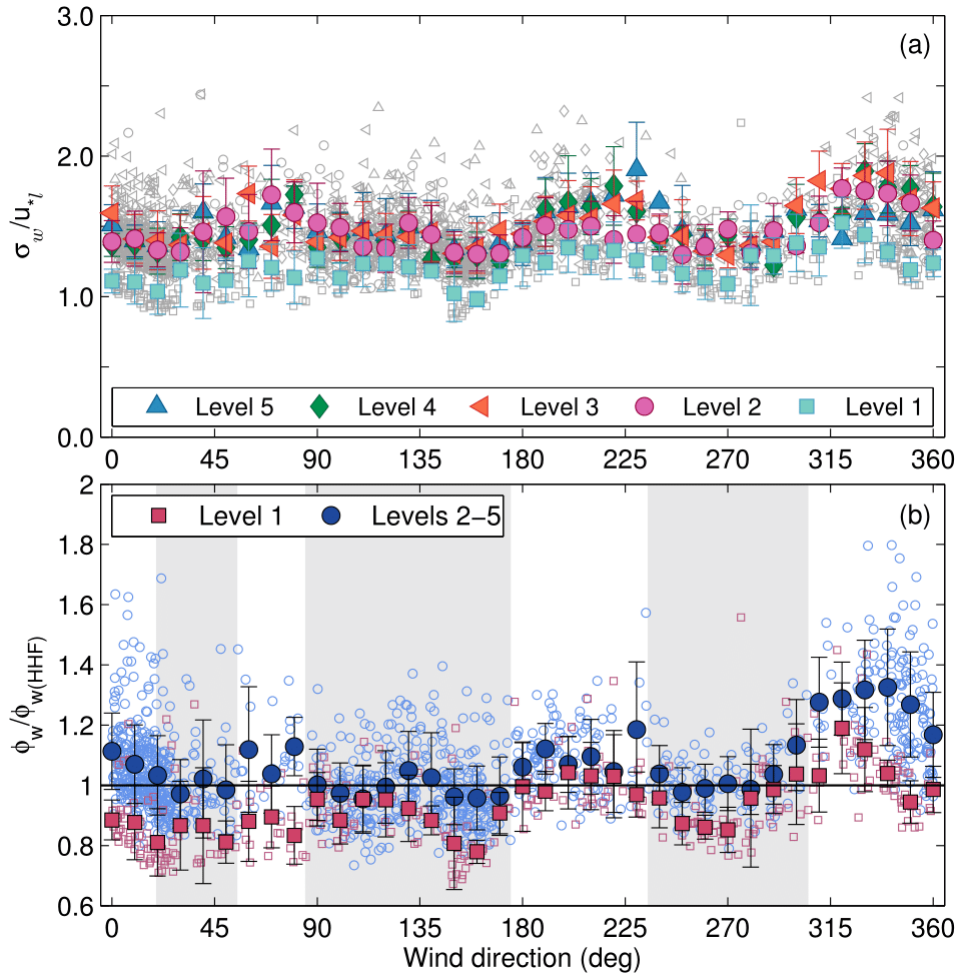
Reference	Site description	σ_u/u_{*l}	σ_v/u_{*l}	σ_w/u_{*l}
Panofsky and Dutton (1984)	Flat (reference)	2.39 ± 0.03	1.92 ± 0.05	1.25 ± 0.03
Rotach (1993)	Urban RSL	2.2	1.5	0.94
Rannik (1998)	Pine forest RSL	2.25 ± 0.31	1.82 ± 0.29	1.33 ± 0.14
Moraes et al. (2005)	Complex (valley)	2.4	2.2	1.2
Wood et al. (2010)	Urban BL	2.36	1.92	1.40
This study – Level 1	Heterogeneous	2.13	1.65	1.11
This study – Levels 2–5	Heterogeneous	2.41	2.08	1.37

464

465 4.1.1. *Influence of the surface heterogeneity*

466 Due to the fact that measurements were performed in a very heterogeneous landscape, we investigated
467 possible influences of different land-use types on turbulence statistics by considering changes for different
468 wind directions. Figure 5a shows the normalized standard deviation of the vertical wind component for each
469 observational level averaged over the entire stability range plotted versus wind direction. For the wind sector
470 45–90 deg there is no consistent increase of σ_w/u_{*l} with height, possibly due to the fact that this narrow
471 wind sector is characterized through a sudden change of surface roughness (from agricultural fields to rough
472 forest) and also through a short fetch (some 70 m). This might indicate a more complex vertical structure
473 than depicted in Fig. 2 with flow which has not reached equilibrium yet. In the 300–360 deg wind sector,
474 the non-dimensional variance of the vertical wind has decreased values at the highest level in comparison
475 with values at levels 2–4. We hypothesize that this might indicate an influence of drainage flows from hills
476 located north of the measurement site. Drainage flows are thermally-driven and they occur during night over
477 sloping terrain often leading to the formation of low level jets. However, we do not have the necessary
478 information to substantiate this hypothesis. In the 190–260 deg sector, σ_w/u_{*l} increases with height
479 indicating the flow which has adjusted to the new surface. This sector has the longest fetch (over 300 m) and
480 highly rough but uniform underlying surface (Figs. 1 and 2).

481 Observed changes of the normalized vertical wind variance with varying wind direction reflect the
482 influence of the surface inhomogeneity (and possibly topography). This influence is seen from the ratio of
483 observed non-dimensional variance of the vertical wind and corresponding values of commonly used
484 similarity formulas for σ_w/u_{*l} in the “ideal” HHF terrain (e.g. Kaimal and Finnigan (1994), $\sigma_w/u_{*l} = 1.25(1$
485 $+ 0.2\zeta)$) in the stability range $0 < \zeta < 1$ (Fig. 5b). We observe that ratio of these two similarity functions at
486 the lowest measurement level is typically less than one, except for the flow from sectors 200–220 deg and
487 300–340 deg, which correspond to high roughness and long fetch (Fig. 1) and high wind speeds (Fig. 3),
488 respectively. At upper levels values of the ratio $\phi_w/\phi_{w(HHF)}$ are larger than unity for wind azimuth ranges
489 55–80 deg, 170–230 deg and 300–360 deg (Fig. 5b). For these levels, the average $\phi_w/\phi_{w(HHF)}$ ratio in
490 Fig. 5b varies between 0.96 and 1.33, which is similar to values obtained by Rannik (1998) in the study over
491 a forest, and the standard deviation for 10 deg wide bins is between 0.08 and 0.22.



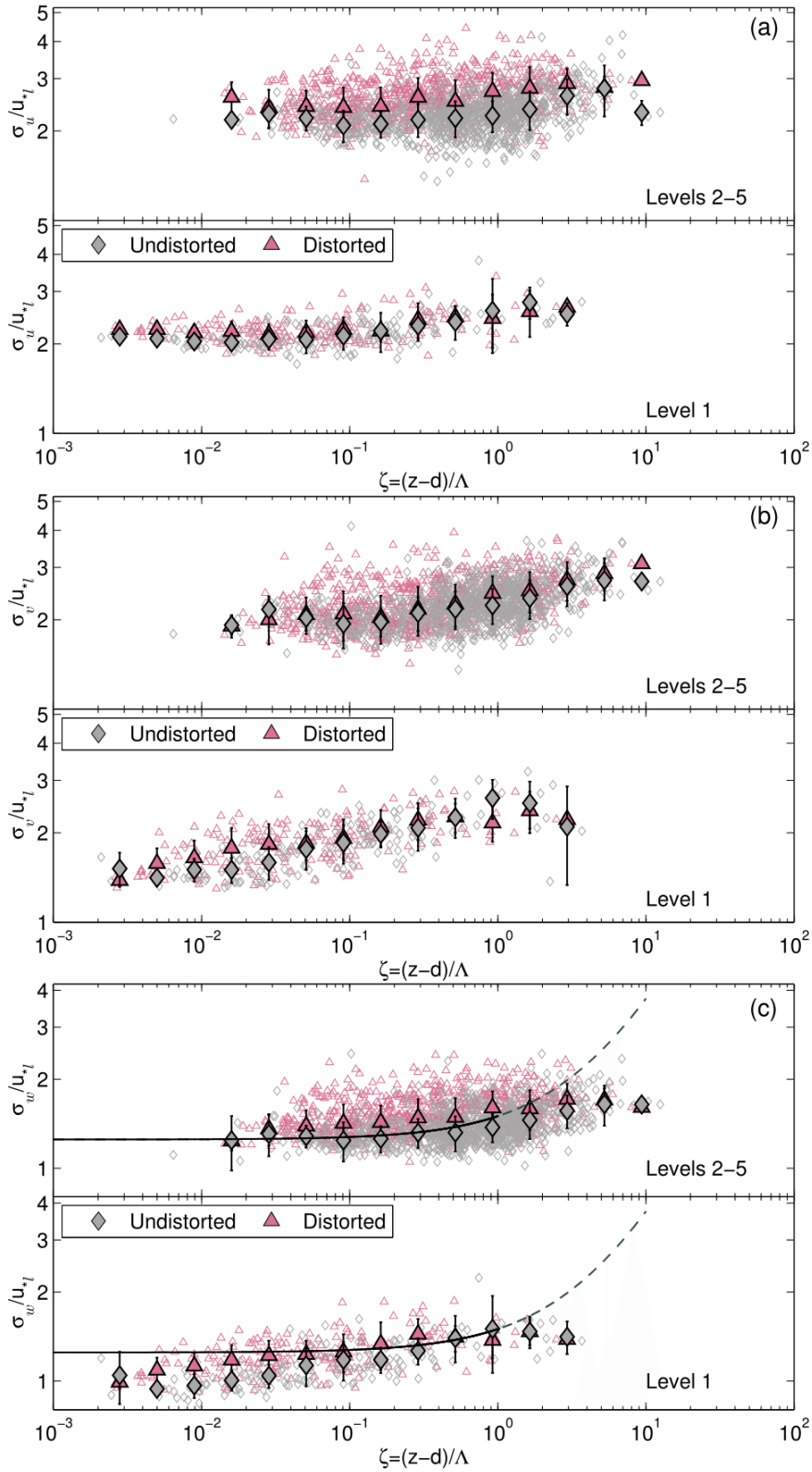
492

493 **Fig. 5.** (a) Scaled standard deviation of vertical velocity fluctuations as a function of wind direction
 494 (regardless of stability). Individual data points at each level corresponding to the particular wind sector are
 495 shown as background symbols. Colored filled symbols correspond to bin averages over the entire stability
 496 range at each observational level. Error bars indicate one standard deviation within each bin. (b) Observed
 497 dimensionless standard deviation of vertical wind speed (for the lowest level and levels 2–5) relative to the
 498 SL similarity prediction for HHF terrain (Kaimal and Finnigan (1994), denoted “HHF”) for stability $0 < \zeta <$
 499 1 , plotted versus wind direction. Shaded light gray areas indicate the wind azimuths which correspond to
 500 undistorted surface conditions ($\phi_w / \phi_{w(HHF)} \approx 1$). These correspond to wind directions 20–55 deg, 85–175
 501 deg and 235–295 deg. The flow from other wind directions is considered as distorted.

502

503 Accordingly, we separately analyzed the velocity variances for different wind directions corresponding
 504 to undistorted and distorted sectors, respectively. Based on $\phi_w / \phi_{w(HHF)} \approx 1$ undistorted wind directions
 505 were defined to correspond to wind directions 20–55 deg, 85–175 deg and 235–295 deg (light gray shaded
 506 area in Fig. 5b). All other wind directions were considered as distorted. The number of data within each
 507 group was nearly evenly distributed except for the highest level. Namely, the percentage of data
 508 corresponding to the undistorted sectors was 47, 56, 54, 52 and 64 % for levels from 1 to 5, respectively.

509 Figure 6 shows all three non-dimensional standard deviations at the lowest level and for levels 2–5 for
510 undistorted and distorted wind direction sectors separately. We note that the scatter is larger for horizontal
511 components than for the vertical wind component. Also, as one might expect the scatter is larger for the
512 distorted sectors compared to undistorted. Normalized variances at level 1 show much less dependence on
513 the wind direction compared to levels 2–5. This reflects the rather local RSL impact that determines the
514 statistics. That is, RSL turbulence appears to be affected by a fetch of less than 100 m from the tower as was
515 estimated by the flux-footprint model (Section 3.2.) rather than by the more distant complex surface.
516 Differences between distorted and undistorted sectors at this level are only found in the near-neutral regime
517 with larger magnitudes for the distorted sectors. For levels 2–5 we observe that the overall shape of the
518 curves for the two sectors is quite similar for all three wind variances. Dimensionless longitudinal and
519 vertical wind variances show higher values in the distorted sectors, while the lateral wind variance seems to
520 be independent on the wind direction. Similar to level 1, the lateral wind component shows a more
521 pronounced increase with stability than the longitudinal and vertical variances. The dimensionless vertical
522 wind variance in the undistorted sectors can be represented quite well with the similarity relationship valid
523 for flat and homogeneous terrain (Kaimal and Finnigan, 1994) in the stability range $0.01 < \zeta < 1$. Based on
524 modeled footprints particular wind sectors were related to corresponding surface types, accordingly. For the
525 undistorted wind directions 20–55 deg and 85–175 deg the underlying surface is represented with
526 agricultural fields, while the 235–295 deg sector represents somewhat rougher but quite uniform surface
527 covered mostly with the forest (Fig. 1). This implies that measurements at levels 2–5 corresponding to these
528 sectors correspond to a layer which is in equilibrium with the underlying surface of more uniform roughness.
529 In the strongly stable regime (for $\zeta > 1$) the normalized variances show a tendency for a leveling-off, thus
530 suggesting that z -less scaling might be appropriate. This implies that even for highly inhomogeneous terrain
531 local scaling appears to be appropriate for all three velocity variances and that the local Obukhov length is
532 relevant length scale. Additionally, in the strong stability limit the z -less scaling seems to be appropriate for
533 longitudinal and vertical wind variances.



534

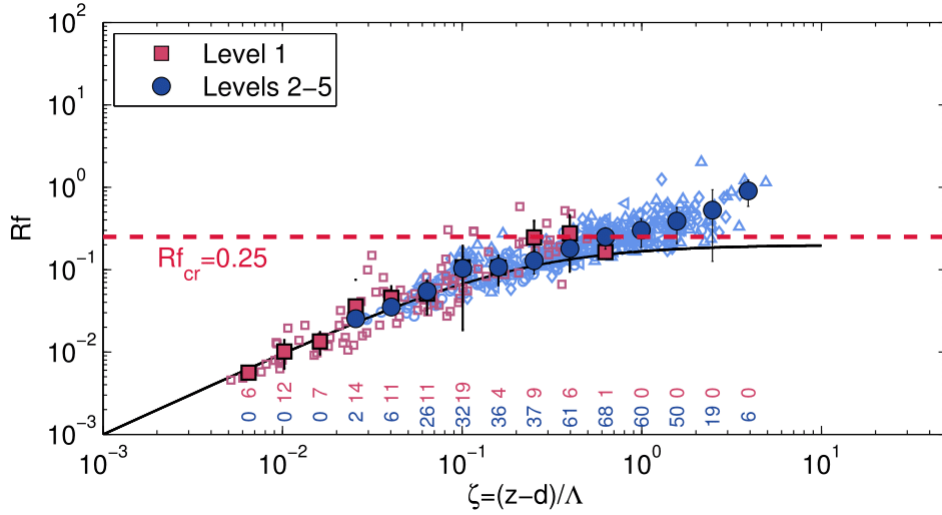
535 **Fig. 6.** Scaled standard deviations of (a) longitudinal, (b) lateral and (c) vertical velocity fluctuations as
 536 functions of stability for level 1 (lower sub-panels) and levels 2–5 (upper sub-panels) for distorted (pink
 537 triangles) and undistorted (gray diamonds) wind sectors. For explanation of other symbols see Fig. 4.
 538

539 4.1.2. *Subcritical and supercritical turbulence regimes*

540 Grachev et al. (2013) showed that the inertial subrange, associated with the Richardson-Kolmogorov
541 cascade, dies out when both the gradient and the flux Richardson number exceed a “critical value” of
542 approximately 0.20 – 0.25, with $Rf_{cr} = 0.20 - 0.25$ being the primary threshold. They argued that a
543 collapse of the inertial subrange is caused by the collapse of energy-containing/flux-carrying eddies. This
544 leads to the invalidity of Kaimal's spectral and cospectral similarity (Kaimal, 1973) and consequently, to
545 violations of flux-profile and flux-variance similarity. Correspondingly, Grachev et al. (2013) classified the
546 traditional SBL into two major regimes: subcritical and supercritical. In the former ($Ri < Ri_{cr}$ and $Rf <$
547 Rf_{cr}), turbulence statistics can be described by similarity theory and it is associated with Kolmogorov
548 turbulence. The supercritical regime ($Ri > Ri_{cr}$ and $Rf > Rf_{cr}$) is related to small-scale, decaying, non-
549 Kolmogorov turbulence, and strong influence of the Earth's rotation even near the surface. Figure 7 shows
550 the dependence of Rf (Eq. (8)) on the local stability parameter at the measuring site. Dyer's parameterization
551 (Dyer, 1974) predicts an asymptotic limit to $Rf_{cr} = 0.2$ (solid black line), but this under-predicts Rf for
552 higher stabilities for which Rf increases above $Rf_{cr} = 0.25$ (supercritical regime). The range of stability
553 available for our analysis of the profile data is $0 < \zeta < 5$. For example, at levels 4 and 5, 40% and 50% of
554 data points have $Rf > Rf_{cr}$, respectively. Thus, higher levels, which correspond to higher stabilities, are
555 characterized by non-Kolmogorov turbulence.

556 Grachev et al. (2013) have found that $Rf_{cr} = 0.20$ was the primary threshold for σ_w/u_{*l} . The
557 normalized standard deviation of the vertical wind speed was reported to become asymptotically constant in
558 the subcritical regime indicating consistency with z -less scaling in this regime. In the supercritical regime
559 σ_w/u_{*l} was monotonically increasing with increasing stability. The turbulence characteristics at our site
560 (exemplified by the vertical velocity variance, Fig. 8) do not show a clear distinction in behavior between
561 sub- and supercritical regimes as was found in Grachev et al. (2013) and for the non-dimensional vertical
562 gradient of mean wind (Fig. 12). In the subcritical regime the number of data points at levels 2–5 with $\zeta > 1$
563 is equal to 25 and is represented by only two bin averages. While Grachev et al. (2013) had a much broader
564 range of stability in both regimes (they obtained z/Λ as small as 0.02 for the supercritical and up to 5 for the
565 subcritical regime, respectively), in our dataset the results for these two regimes are almost indistinguishable
566 (Fig. 8). Additionally, for the supercritical regime Grachev et al. (2013) observed an

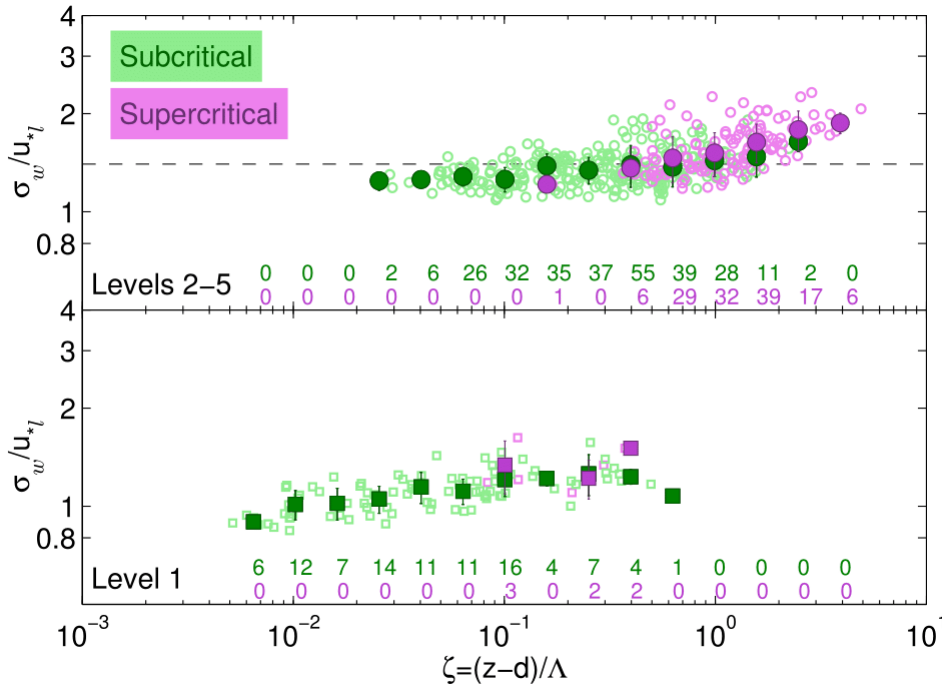
567



568

569 **Fig. 7.** Stability dependence of the flux Richardson number for all five levels (shown with corresponding
 570 symbol). Red squares and blue circles denote bin averages for the lowest level and for levels 2–5,
 571 respectively. Error bars indicate one standard deviation within each bin. Number of data points inside each
 572 bin for the two subsets of the data is also given.

573



574

575 **Fig. 8.** Scaled standard deviation of vertical velocity fluctuations as a function of stability. Data from the
 576 lowermost level (squares) and for levels 2–5 (circles) in the subcritical (green) and supercritical (violet)
 577 regime are presented. The dashed line is equal to 1.4 which is the mean value of all data for levels 2–5 in the
 578 subcritical regime. The number of data in each regime is indicated with the corresponding color.

579

580 increase of σ_w/u_{*l} in the range $3 < \zeta < 100$. For this regime we observed an increasing tendency for the two
 581 highest levels, but this is probably not significant because of the small number of data and a restricted

582 stability range (upper limit is $\zeta = 5$). Note that the number of data points here is much less compared to Figs.
 583 4 and 6 because only 100 simultaneous 30-min intervals were available for the calculation of the flux
 584 Richardson number. Similar results are found for the horizontal wind variances (not shown).

585

586 4.2. Turbulent kinetic energy

587 Estimation of turbulent kinetic energy (TKE) is very important for atmospheric numerical modeling,
 588 since turbulent mixing is often parameterized using TKE. Here we investigate the TKE, defined as, $e =$
 589 $\frac{1}{2}(\overline{u'^2} + \overline{v'^2} + \overline{w'^2})$, which represents a turbulent kinetic energy per unit mass (Stull, 1988). Fig. 9 shows e
 590 scaled by the squared friction velocity. In numerical models which use 1.5-order closure or TKE closure,
 591 TKE is predicted with a prognostic energy equation, and eddy viscosity is specified using the TKE and some
 592 length scale. Since TKE is essentially the sum of variances (divided by 2), according to Kansas values for
 593 neutral conditions (Kaimal and Finnigan, 1994), the value of scaled TKE is equal to 5.48 for HHF terrain.

594 Over HHF terrain in Antarctica, Sanz Rodrigo and Anderson (2013) found that for neutral to moderate
 595 stabilities non-dimensional TKE is roughly constant up to $\zeta = 0.5$. Above this value, non-dimensional TKE
 596 grows until it reaches $\zeta = 10$ (corresponding to the boundary-layer top), which is followed by an asymptotic
 597 value for stronger stabilities (Fig. 9, dashed black line, Eq. (14)). They proposed a simple empirical
 598 parameterization:

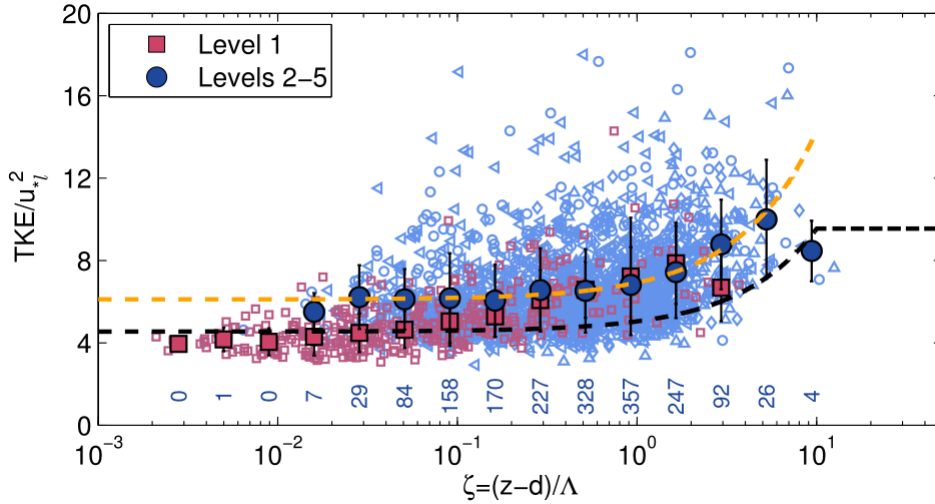
$$\frac{TKE}{u_{*l}^2}(\zeta) = \begin{cases} \frac{1}{\alpha_0} + b_E \zeta, & \zeta \leq 10 \\ \frac{1}{\alpha_0} + b_E 10, & \zeta > 10 \end{cases} \quad (14)$$

599 where $\alpha_0 = 0.22$ is the neutral limit value and $b_E = 0.5$.

600 We fitted the above linear relation to our data from levels 2–5 in the stability range $0.006 < \zeta < 8.30$
 601 (Fig. 9, orange dashed line) using the least-squares method. Figure 9 shows a clear influence of the RSL on
 602 the lowest measurement level, which does not correspond to the proposed near-linear expression (14). The
 603 RSL influence also results in a reduced value of non-dimensional TKE for the neutral range ($TKE/u_{*l}^2 \approx$
 604 4.25 based on values from Tab. 4) in comparison with the value of 4.5 found by Sanz Rodrigo and Anderson
 605 (2013). Their value is smaller than the reference value of 5.48 for HHF terrain probably due to higher air
 606 density in the Antarctica causing reduced values of TKE/u_*^2 compared to mid-latitudes. We note that the
 607 relation of the type given by Eq. (14) fits our data for levels 2–5 quite well (Fig. 9, orange dashed curve),

608 but with slightly different coefficients $\alpha_0 = 0.16$, which corresponds to a neutral value of $TKE/u_*^2 = 6.1$,
 609 and $b_E = 0.8$. The fitted neutral value of dimensionless TKE for levels 2–5 is close to the value of 6.01,
 610 which is obtained based on values from Tab. 4.

611



612

613 **Fig. 9.** Dependence of non-dimensional turbulent kinetic energy on stability. The black dashed line is an
 614 empirical fit (Eq. (14), Sanz Rodrigo and Anderson (2013)). Individual data at each level are shown in
 615 background symbols, while red squares and blue circles represent bin-averages for the lowest and four
 616 higher levels, respectively. Error bars indicate one standard deviation within each bin. The number of data
 617 points within each bin for levels 2–5 is also indicated. The orange curve is a fit to our data for levels 2–5.

618

619 Similar to wind variances, analysis of the TKE with respect to wind direction shows similar distinction
 620 between the distorted and undistorted sectors. While values of normalized TKE are similar for the two
 621 sectors at the lowest level, at levels 2–5 magnitudes in the distorted sectors are larger. The dependence of
 622 TKE/u_*^2 on the stability parameter can be represented with a linear relationship, but the best fit coefficients
 623 are somewhat changed: $\alpha_0 = 0.19$ and 0.14 and $b_E = 0.97$ and 0.95 for undistorted and distorted sectors,
 624 respectively (not shown). The behavior of the normalized TKE in the sub- and supercritical regime was
 625 found to be consistent with the behavior of the normalized wind variances and no discernible difference
 626 between these two regimes was observed (not shown).

627 4.3. Correlation coefficients

628 In order to estimate fluxes from mean wind and temperature as inputs for dispersion models it is useful
 629 to use turbulent correlation coefficients. These coefficients are a measure of the efficiency of turbulent
 630 transfer and are defined as

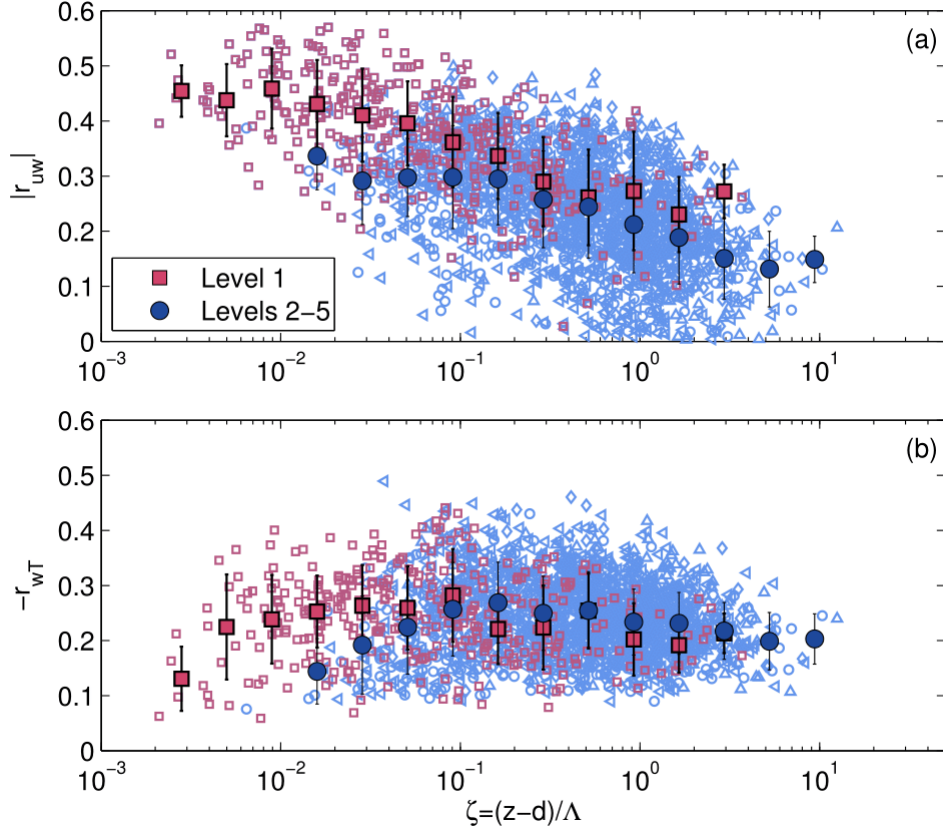
$$r_{uw} = \frac{\overline{u'w'}}{\sigma_u \sigma_w} \quad (15)$$

$$-r_{wT} = \frac{\overline{w'\theta'_v}}{\sigma_w \sigma_{\theta_v}} \quad (16)$$

631 where r_{uw} and r_{wT} are correlation coefficients for momentum and heat transfer, respectively. Figure 10
 632 shows momentum and heat flux correlation coefficients estimated for the lowest and the four higher
 633 measurement levels. For strong stratification we obtained smaller values of the correlation coefficients for
 634 momentum, but they increase quite steeply while approaching neutral conditions. This was also observed in
 635 both an urban (e.g. Wood et al., 2010) and a rural dataset (e.g. Conangla et al., 2008). Additionally, r_{uw}
 636 exhibits the same behavior with respect to the stability when analyzed for different wind azimuths. The
 637 magnitude of the momentum correlation coefficient is larger for the undistorted sector compared to distorted
 638 in the stability range $0 < \zeta < 1$ in the whole measurement layer (not shown). The stability-averaged
 639 momentum flux correlation coefficient values are between 0.23 and 0.46 at level 1 (Fig. 10a) and a similar
 640 range was observed for undistorted (0.22–0.51) and distorted (0.25–0.45) wind sectors. These values are
 641 similar to those obtained by Marques Filho et al. (2008). For levels 2–5, the values of r_{uw} are somewhat
 642 smaller compared to level 1 and are in the range 0.14–0.34 (Fig. 10a), and they are similar to those obtained
 643 for the distorted wind sectors: 0.16–0.31 (not shown), which is in the range of values observed over
 644 generally rougher urban surfaces (Wood et al., 2010).

645 The correlation coefficient for heat exhibits larger values for $\zeta > 0.1$ for levels 2–5, and it decreases
 646 while approaching neutral conditions. The correlation coefficient for heat is between 0.10 and 0.26, which is
 647 similar to values reported in other studies (Marques Filho et al., 2008; Wood et al., 2010). Additionally, no
 648 discernible dependence on wind direction was found for r_{wT} mostly due to the large scatter of the data (not
 649 shown). Mean values of the momentum and heat flux correlation coefficients over the entire measurement
 650 layer, and for all stabilities, are equal to 0.26 and 0.24, respectively. Also, no discernible difference in

651 behavior of the momentum and heat flux correlation coefficients was observed between the sub- and
 652 supercritical regimes (not shown).
 653



654
 655 **Fig. 10.** Momentum (a) and heat flux (b) correlation coefficients plotted as a function of stability.
 656 Background symbols represent individual data at each level while red squares and blue circles show bin-
 657 averages for the first level and for levels 2–5, respectively. Error bars indicate one standard deviation
 658 corresponding to the particular bin.

659
 660 *4.4. Flux-gradient similarity*

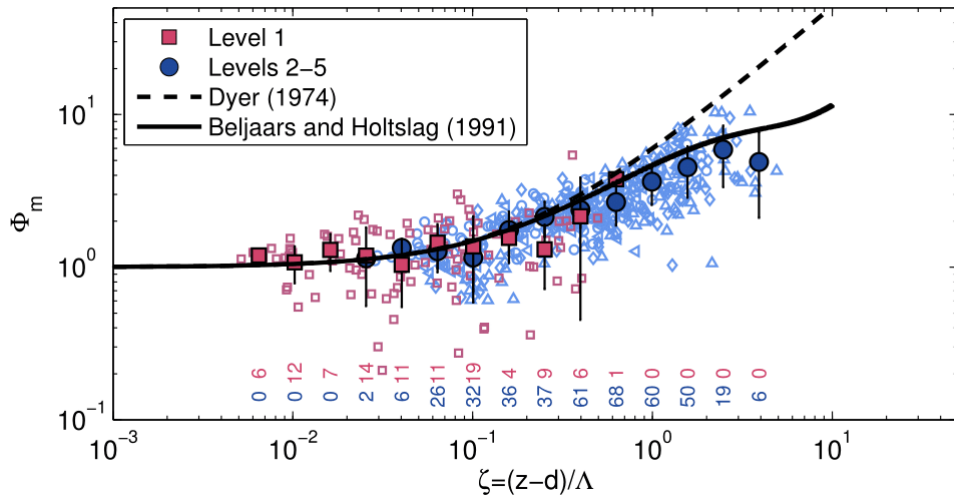
661 We also investigated the relationship between mean vertical gradients and turbulent fluxes, also known
 662 as the flux-gradient relationships. Several interpolation methods were tested in order to determine the mean
 663 wind profile, and the second order polynomial fit was found to best fit the observed data. Thus, the vertical
 664 gradient of mean wind speed is obtained by fitting a second order polynomial through the 30-min measured
 665 profiles

$$U(z) = p_1 \left[\ln \left(\frac{z-d}{z_0} \right) \right]^2 + p_2 \ln \left(\frac{z-d}{z_0} \right) + p_3 \quad (17)$$

666 and by evaluating a derivative with respect to z for each measurement level. The second order polynomial fit
667 is widely used for measurements within the roughness sublayer (e.g. Dellwik and Jensen, 2005; Rotach,
668 1993) as well as within the inertial sublayer (e.g. Forrer and Rotach, 1997; Grachev et al., 2013). Only about
669 one hundred simultaneous 30-min intervals were available from each measurement level for the profile
670 analysis. Results of the variance and TKE analyses showed a different behavior of the first level in
671 comparison with all the others. In order to investigate whether there is a difference in the flux-gradient
672 relationship as well, the data from the first level and levels 2–5 are presented separately (Fig. 11). For our
673 dataset no discernible difference of ϕ_m between level 1 and levels 2–5 can be observed. Almost all data at
674 the first measurement level are within the stability range $z/\Lambda < 0.5$ and ϕ_m tends to a constant value of 1
675 when approaching near-neutral conditions. Quite diverse results concerning the value of ϕ_m in the RSL in
676 the near-neutral conditions can be found in the literature. While in some studies of flux-gradient similarity
677 within the forest RSL, ϕ_m was found to be less than unity in the near-neutral range (e.g. Högström et al.,
678 1989; Mölder et al., 1999; Raupach, 1979; Thom et al., 1975), other studies indicate that ϕ_m is close to unity
679 (e.g. Bosveld, 1997; Simpson et al., 1998; Dellwik and Jensen, 2005; Nakamura and Mahrt, 2001). Bosveld
680 (1997) found that momentum and heat eddy diffusivities differ in magnitude in neutral conditions. This
681 means that, with increasing canopy density, heat exchange remains enhanced in the RSL, whereas
682 momentum exchange approaches surface-layer values. Dellwik and Jensen (2005) observed an increase of
683 ϕ_m in the RSL in neutral conditions over fetch-limited deciduous forest due to the increased wind gradients
684 directly above the canopy top. In previous studies reporting $\phi_m < 1$ and having mostly been conducted over
685 pine forests (which compared to a closed deciduous forest have less biomass in the top of the canopy) the
686 observed wind profile close to the three tops was less steep.

687 The previous sections have revealed clear differences in the flux-variance relationships between level 1 and
688 levels 2-5 (i.e., the RSL and the transition layer, respectively) at the present site. In contrast, no significant
689 difference is observed for the flux-gradient relationship. Similar results were reported by Katul et al. (1995)
690 who pointed out that inhomogeneity in the RSL impacts variances but not necessarily fluxes. Following this
691 line, our results seem to indicate that surface characteristics at our site are influencing the strength of
692 turbulent mixing and the wind gradient in the same way. This conclusion is additionally corroborated by the
693 results of the analysis for different wind sectors as no dependence on the wind direction was found for the
694 non-dimensional gradient of wind speed (not shown).

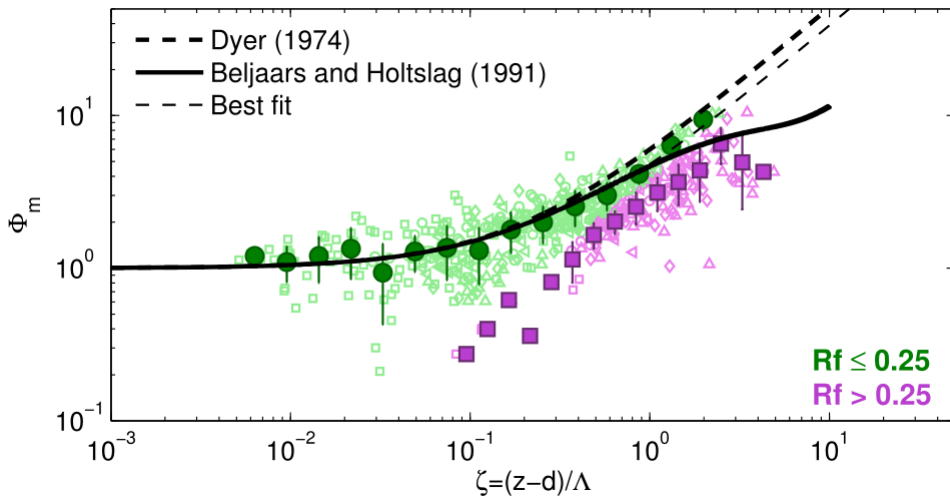
695 According to Fig. 11, ϕ_m increases more slowly with increasing stability than predicted by the linear
696 approach (Eq. (6), dashed black line) and it appears to closely follow the Beljaars-Holtslag function (Eq.
697 (7)). The Beljaars-Holtslag formulation reduces the overestimation of the non-dimensional gradients for very
698 stable conditions (Fig. 11, black solid line). Similar results were also obtained by other studies. For example,
699 Mahrt (2007) found that ϕ_m increases linearly only up to 0.6, while in the range $0.6 < \zeta < 1.0$ it increases
700 more slowly than the linear prediction. However, according to Grachev et al. (2013) this result brings into
701 question z -less scaling. Assuming that ϕ_m is a linear function of stability, the gradients should tend to
702 constant values for $\zeta \gg 1$. Thus, the leveling-off of the ϕ_m at large stabilities is an evidence for the
703 breakdown of z -less stratification. Grachev et al. (2013) hypothesized that the leveling-off of ϕ_m functions
704 for strong stability may be due to including data for which local similarity is not applicable into the analysis.
705



706
707 **Fig. 11.** Non-dimensional vertical gradient of the wind speed plotted versus the local stability parameter.
708 Individual data points for each level are shown in the corresponding symbol (as in Fig. 4), while data from
709 the lowest level are indicated with red color and from levels 2–5 in blue color. Dashed line corresponds to
710 the linear relationship of Dyer (1974)(Eq. (6)) and the solid line is Beljaars and Holtslag (1991) relationship
711 (Eq. (7)). Bin averages for the lowest and four higher levels are included for easier interpretation of results.
712 Error bars indicate one standard deviation within each bin. Number of data points in each bin is also shown.
713

714 Following the approach of Grachev et al. (2013), we imposed the prerequisite $Rf < Rf_{cr} = 0.25$ on all
715 individual data at each level. According to Fig. 12, data with $Rf < 0.25$ almost perfectly follow the linear
716 dependence on stability (according to Eq. (6)) with the best-fit coefficient $b_E = 3.8$ (thin dashed line in Fig.
717 12). This implies the consistency of the data with the z -less prediction. The behavior of the non-dimensional

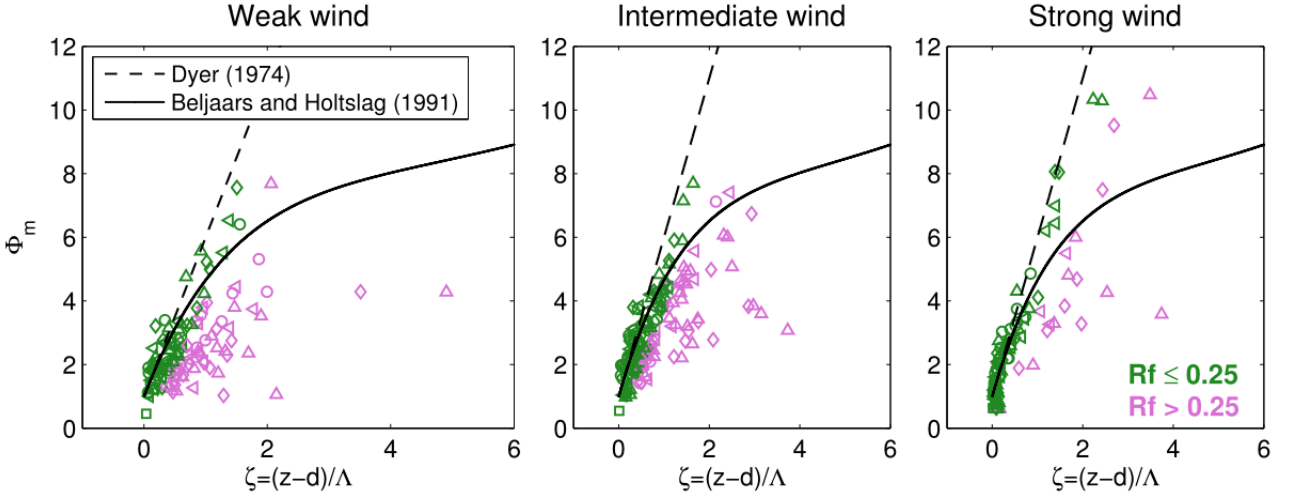
718 gradient of wind speed in the supercritical regime in Fig. 12 exhibits a large deviation from the linear
 719 similarity prediction in the entire stability range. Moreover, supercritical data have a tendency to level-off.
 720 This suggests that the Beljaars-Holtstag non-linear expression (Eq. (7), Beljaars and Holtstag, 1991), as well
 721 as the results from other studies which exhibited leveling-off of similarity functions (e.g. Baas et al., 2006;
 722 Forrer and Rotach, 1997; Grachev et al., 2013, 2007) were most likely affected by a large number of small-
 723 scale, non-Kolomogorov turbulence data.
 724



725
 726 **Fig. 12.** The non-dimensional vertical gradient of wind speed plotted versus stability for two different
 727 regimes: subcritical ($Rf \leq 0.25$, green) and supercritical ($Rf > 0.25$, violet). Error bars indicate one
 728 standard deviation within each bin. Thick dashed line indicates the linear relationship (6) (Dyer, 1974); the
 729 thin dashed line is the best fit to our data for $Rf \leq 0.25$ (in the stability range $0.005 < \zeta < 2.43$), while the
 730 bold solid line corresponds to Eq. (7) (Beljaars and Holtstag, 1991).
 731

732 Ha et al. (2007) evaluated surface layer similarity theory for different wind regimes in the nocturnal
 733 boundary layer based on the CASES-99 data. They concluded that although the stability parameter is
 734 inversely correlated to the mean wind speed, the speed of the large-scale flow has an independent role on the
 735 flux-gradient relationship. For strong and intermediate wind classes, they found that ϕ_m obeyed existing
 736 stability functions when z/L is less than unity, while for weak mean wind and/or strong stability ($z/L > 1$)
 737 similarity theory broke down. Following their approach, we evaluated the flux-gradient relationship
 738 separately for different wind regimes, which were classified based on the mean wind speed at each level
 739 similarly as in the study of Ha et al. (2007), and discriminated between subcritical and supercritical regimes.
 740 The striking difference of the behavior of ϕ_m with stability for different wind classes, which was found in

741 the study of Ha et al. (2007), cannot be observed in our dataset (Fig. 13). In the weak wind regime the scatter
 742 is largest, although we have noted substantial scatter even for the intermediate and strong classes, caused by
 743 the small scale turbulence, which survived even in the supercritical regime (violet symbols). If we consider
 744 only data for $Rf \leq 0.25$, they follow Dyer's linear prediction even for the weak wind regime, indicating that
 745 similarity theory holds in this regime for the whole range of stabilities.
 746



747
 748 **Fig. 13.** Non-dimensional vertical gradient of wind speed for each level plotted versus local stability
 749 parameter for weak-, intermediate- and strong wind regimes, respectively. Individual data points for each
 750 level are shown with the corresponding symbol. Data points exceeding critical value of $Rf_{cr} = 0.25$
 751 (supercritical regime) are shown in violet. Dashed line indicates the linear relationship of Dyer (1974) (Eq.
 752 (6)) and the solid line corresponds to the relationship (7) (Beljaars and Holtslag, 1991).
 753

754 We now turn to the self-correlation analysis. Since the present data exhibit different behavior for the
 755 subcritical and supercritical regimes, the self-correlation analysis was performed separately for each of these
 756 regimes. Linear correlation coefficients between ϕ_m and ζ for the original data and random data sets were
 757 calculated for each level. Table 5 shows the impact of self-correlation on the dimensionless wind shear.
 758 Generally, the results for both the sub- and supercritical regimes suggest a non-negligible but not decisive
 759 impact of self-correlation. There are, however, two exceptions. At the lowest level, the subcritical data
 760 mostly reflect the near-neutral range where large scatter of the data is present resulting in a relatively small
 761 correlation coefficient of 0.54. Hence the self-correlation test, which is based on linear correlation, produces
 762 small correlations of similar magnitudes for both physical and random data. This in turn results in a very
 763 small value of $R_{data}^2 - \langle R_{rand}^2 \rangle$ which means that results of this test are not very conclusive. At level 5, the

764 correlation coefficient is large in the subcritical regime and reduced in the supercritical due to the increased
765 scatter of the data for $\zeta > 1.5$ in this regime. Consequently, the value of $R_{data}^2 - \langle R_{rand}^2 \rangle$ is small. For the
766 three middle levels, R_{data} has similar values in both the subcritical and supercritical regime, since in both
767 regimes they exhibit a strong positive fit, i.e. ϕ_m increases with increasing stability with the larger scatter
768 observed at level 4 (Fig. 12).

769

770 **Table 5**

771 Self-correlation analysis. R_{data} is a linear correlation coefficient between ϕ_m and ζ for the original data at
772 each level. $\langle R_{rand} \rangle$ is the self-correlation and it is the average of the correlation coefficients for 1000
773 random datasets. $R_{data}^2 - \langle R_{rand}^2 \rangle$ is a measure of the true physical variance explained by the linear model
774 as proposed by Klipp and Mahrt (2004). Standard deviations are also indicated. N is the number of 30-min
775 intervals.

Subcritical	N	R_{data}	$\langle R_{rand} \rangle$	$\sigma \langle R_{rand} \rangle$	$R_{data}^2 - \langle R_{rand}^2 \rangle$	$\sigma(R_{data}^2 - \langle R_{rand}^2 \rangle)$
Level 1	93	0.54	0.51	0.14	0.01	0.14
Level 2	83	0.91	0.55	0.11	0.50	0.12
Level 3	78	0.95	0.49	0.11	0.64	0.11
Level 4	60	0.73	0.49	0.13	0.28	0.13
Level 5	52	0.97	0.49	0.14	0.68	0.13
Supercritical						
Level 1	7	0.91	0.68	0.22	0.33	0.25
Level 2	17	0.91	0.51	0.18	0.54	0.18
Level 3	22	0.92	0.55	0.18	0.51	0.19
Level 4	39	0.66	0.43	0.15	0.22	0.13
Level 5	48	0.57	0.41	0.14	0.14	0.12

776

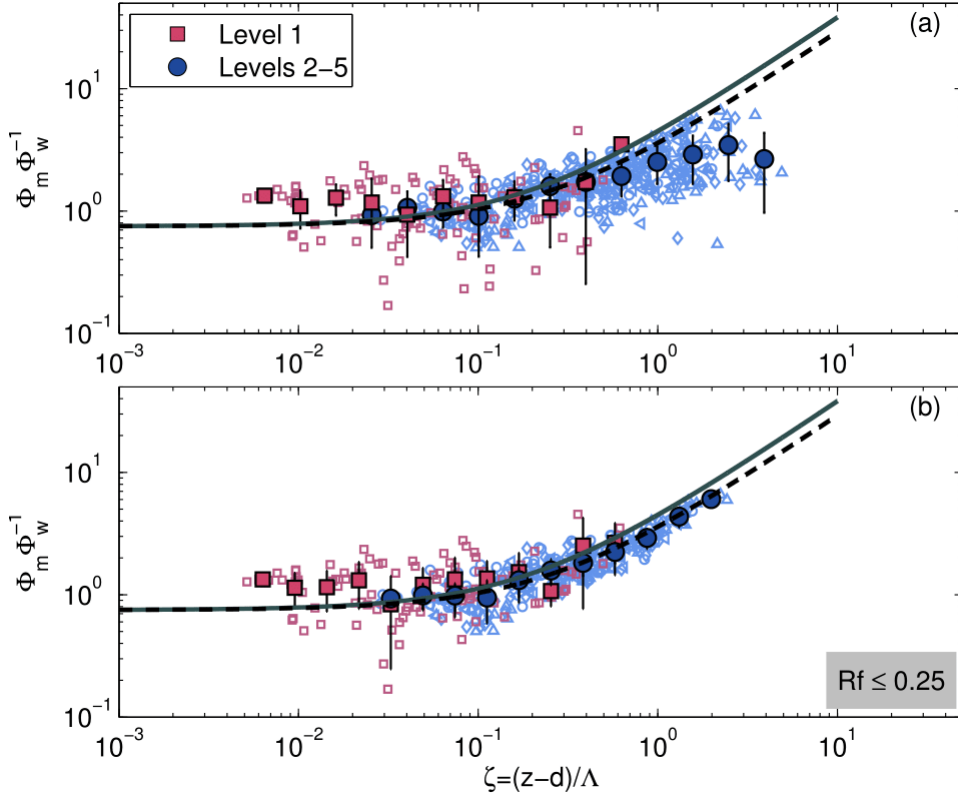
777

778 Grachev et al. (2013) proposed a new method which is not influenced by self-correlation and for which
779 z -less scaling should also be valid. This new function represents a combination of universal functions and is
780 thus a universal function itself. This new function,

$$\phi_m \phi_w^{-1} = 0.75(1 + 5\zeta) \quad (18)$$

781 where the value of $\phi_w = 1.33$ corresponds to the median value in the subcritical regime found in the study
782 of Grachev et al. (2013) (Fig. 14, gray solid line). For our data, the median ϕ_w value for levels 2–5 was also
783 found to be equal to 1.33 in the subcritical regime. According to Fig. 14a, the increase of $\phi_m \phi_w^{-1}$ with
784 stability is slower than the linear prediction (solid and dashed lines, respectively). Due to the fact that this
785 new similarity function $\phi_m \phi_w^{-1}$ shares no variable with the stability parameter (except the reference height
786 $z-d$), the observed decrease below the linear prediction is not caused by self-correlation. As seen from Fig.
787 14b, this deviation from the linear relationship is mainly due to the small scale turbulence in the supercritical

788 regime ($Rf > 0.25$). Additionally, this function is consistent with the z -less scaling when the prerequisite
 789 $Rf \leq 0.25$ is imposed on the data (Fig. 14b). As already noted, the RSL shows a more pronounced influence
 790 on the ϕ_w profile compared to the wind shear profile, thus leading to an overestimation of Eq. (18) at level 1
 791 while no systematic deviation can be observed for levels 2–5 (Fig. 14). The scatter in the near-neutral range
 792 at level 1 could be partly due to the wind direction inhomogeneities (not shown).
 793



794
 795 **Fig. 14.** The bin-averaged non-dimensional function $\phi_m \phi_w^{-1} = \frac{k(z-d)}{\sigma_w} \frac{dU}{dz}$, which is not influenced by self-
 796 correlation, plotted versus local stability. Individual data for each level are shown in the corresponding
 797 symbol as in Fig. 4. Bin averages for the lowest level (red squares) and four higher levels (blue circles) are
 798 included for easier interpretation of trends. Error bars indicate one standard deviation within each bin. Gray
 799 line corresponds to the experimental fit according to Grachev et al. (2013) ($\phi_m \phi_w^{-1} = 0.75(1 + 5\zeta)$) and the
 800 dashed black line is the best fit to our data ($\phi_m \phi_w^{-1} = 0.75(1 + 3.8\zeta)$) in the subcritical regime. (b) Same
 801 as (a) but subject to the condition $Rf \leq 0.25$.
 802

803 5. Summary and Conclusions

804 Multi-level measurements of atmospheric turbulence carried out over a heterogeneous surface in the
 805 continental part of Croatia have been used to study turbulence characteristics in the wintertime nocturnal
 806 boundary layer. Measurements that were obtained from five levels in the layer between 20 and 62 m above

807 the ground and 2–44 m above the local canopy height, provided valuable insight in the turbulence
808 characteristics within tens of meters above the ground level. We focused on evaluating the applicability of
809 local similarity scaling approach, in terms of flux-variance and flux-gradient similarity, over spatially
810 inhomogeneous surface characteristics.

811 Due to specific local terrain characteristics and distinctive features of the stable boundary layer (SBL),
812 special attention was given to data quality control and post-processing options, which included
813 determination of appropriate turbulence averaging time scale for defining turbulence fluctuations, testing the
814 stationarity of the data and invoking an uncertainty test. Observations were conducted inside (the lowest
815 observational level) and above the roughness sublayer (RSL).

816 After removing highly uncertain data points (uncertainty threshold > 50 %), when assessing scaling
817 under inhomogeneous fetch conditions in the SBL, dimensionless standard deviations of wind velocity
818 components were found to behave differently than the dimensionless wind shear. Concerning the normalized
819 standard deviations, it was found that vertical velocity shows a tendency to “ideal” behavior, that is, it
820 follows z -less scaling when approaching large stability. The longitudinal and transversal components show a
821 dependency on stability, with the latter exhibiting a more pronounced linear increase with increasing
822 stability. Consequently, scaled turbulent kinetic energy was found to have a linear dependence on the
823 stability parameter in the range $0.05 \leq \zeta \leq 10$ for levels above the RSL. However, we found local scaling
824 to be valid for all three variables, which is astonishing given the complex and spatially inhomogeneous
825 surface characteristics. For neutral conditions, due to the RSL influence values of all three non-dimensional
826 velocity variances were found to be smaller at the lowest measurement level, while these were larger at
827 higher levels in comparison with values obtained for HHF terrain.

828 The ratio of the observed dimensionless standard deviation of the vertical wind component and
829 corresponding values of commonly used similarity formulas over horizontally homogeneous and flat (HHF)
830 terrain showed considerable variation with wind direction, indicating the influence of surface roughness
831 changes and topography. Therefore, we separately analyzed velocity variances for different wind directions
832 corresponding to undistorted ($\phi_w/\phi_{w(HHF)} \approx 1$) and distorted ($\phi_w/\phi_{w(HHF)} \neq 1$) sectors, respectively.
833 Differences between these sectors at the lowest level were only found in the near-neutral regime with larger
834 magnitudes for the distorted sectors. At upper levels, dimensionless longitudinal and vertical wind variances
835 also showed higher values for these wind directions. However, this did not influence results regarding the

836 relationship with stability. For non-dimensional velocity variances, and consequently non-dimensional TKE
837 and the momentum and heat flux correlation coefficients, no discernible difference between sub- and
838 supercritical regimes was observed.

839 Results for the non-dimensional wind shear appear to be less sensitive to inhomogeneous site
840 characteristics. Despite the largely inhomogeneous surface characteristics at the measuring site, flux-gradient
841 relationship showed a similar distinction between Kolmogorov and non-Kolmogorov turbulence as found
842 under ideal (HHF) conditions (Grachev et al., 2013). Our results support the classical Businger-Dyer linear
843 expression for the non-dimensional profile of wind speed, with slightly different best-fit coefficient, even
844 over inhomogeneous terrain but only after removing data which correspond to the flux Richardson number
845 $Rf > 0.25$. Hence, our data follow local z -less scaling for the ϕ_m function when the condition $Rf = 0.25$ is
846 imposed. Similar to HHF conditions, supercritical ($Rf > 0.25$) data show a leveling-off for ϕ_m at higher
847 stability thus seemingly supporting the non-linear relationship of Beljaars and Holtslag (1991). Therefore,
848 we conclude that the non-dimensional wind shear over a largely heterogeneous vegetated surface is only
849 weakly, if at all, affected by the surface inhomogeneity. Thus, when interested in only subcritical, fully
850 turbulent conditions, the classical linear formulation for ϕ_m is appropriate. Correspondingly, if all
851 turbulence states (regardless of sub- or supercritical) are of interest, the Beljaars-Holtslag formulation is to
852 be preferred. Finally, we investigate whether the wind magnitude has an impact on the distinction between
853 Kolmogorov and non-Kolmogorov turbulence. The flux-gradient dependence on stability did not show
854 different behavior for different wind regimes, indicating that the stability parameter is sufficient predictor for
855 flux-gradient relationship.

856 Overall, the present stable night-time results from a forested site with highly inhomogeneous fetch
857 conditions show that flux-variance relationships obey local scaling but the corresponding non-dimensional
858 functions do not exhibit the same parameter values as over HHF terrain. The z -less limes for strong stability
859 is assumed by the vertical and to somewhat lesser degree by the horizontal velocity fluctuations. The RSL
860 influence appears to be larger than the distortion due to inhomogeneous surface conditions. Flux-gradient
861 relationships, on the other hand, seem to be less influenced by surface inhomogeneity: they exhibit the same
862 distinction into sub- and supercritical turbulence regimes as over HHF terrain. For both, subcritical
863 turbulence alone and “all conditions” the data follow quite closely the respective functions from the
864 literature. Finally, no distinct impact of the RSL can be observed for the flux-gradient relations.

866 **Acknowledgements:** We would like to acknowledge Željko Večenaj's crucial role in the setting up
 867 instruments and maintenance of the measurement site. We are also thankful for his assistance in the
 868 application of MFD and stationarity analysis. We are grateful to Branko Grisogono for providing two sonic
 869 anemometers for the use in this experiment. We gratefully acknowledge two anonymous reviewers whose
 870 comments led to the improvement of the manuscript. The study was supported by the Croatian Ministry of
 871 Science, Education and Sports (grant No. 119-1193086-1323). The first author's research visit at Institute of
 872 Atmospheric and Cryospheric Sciences, University of Innsbruck was supported by the Austrian Federal
 873 Ministry of Science, Research and Economy (BMWFW) through Ernst Mach Grant – Worldwide program.

875 **References**

- 876 Andreas, E.L., Hill, R.J., Gosz, J.R., Moore, D.I., Otto, W.D., Sarma, A.D., 1998a. Statistics of
 877 surface-layer turbulence over terrain with metre-scale heterogeneity. *Boundary-Layer*
 878 *Meteorol.* 86, 379–408. doi:10.1023/A:1000609131683
- 879 Aubinet, M., Vesala, T., Papale, D., 2012. *Eddy Covariance: A Practical Guide to Measurement*
 880 *and Data Analysis*. Springer.
- 881 Baas, P., Steeneveld, G.J., van de Wiel, B.J.H., Holtslag, A.A.M., 2006. Exploring self-correlation
 882 in flux-gradient relationships for stably stratified conditions. *J. Atmos. Sci.* 63, 3045–3054.
 883 doi:10.1175/JAS3778.1
- 884 Babić, K., Klaić, Z.B., Večenaj, Ž., 2012. Determining a turbulence averaging time scale by Fourier
 885 analysis for the nocturnal boundary layer. *Geofizika* 29, 35–51.
- 886 Babić, N., Večenaj, Ž., De Wekker, S.F.J., 2016. Flux–variance similarity in complex terrain and
 887 its sensitivity to different methods of treating non-stationarity. *Boundary-Layer Meteorol.* 159,
 888 123–145. doi:10.1007/s10546-015-0110-0
- 889 Basu, S., Porté-Agel, F., Fofoula-Georgiou, E., Vinuesa, J.F., Pahlow, M., 2006. Revisiting the
 890 local scaling hypothesis in stably stratified atmospheric boundary-layer turbulence: An
 891 integration of field and laboratory measurements with large-eddy simulations. *Boundary-*
 892 *Layer Meteorol.* 119, 473–500. doi:10.1007/s10546-005-9036-2
- 893 Beljaars, A.C.M., Holtslag, A.A.M., 1991. Flux parameterization over land surfaces for
 894 atmospheric models. *J. Appl. Meteorol.* doi:10.1175/1520-
 895 0450(1991)030<0327:FPOLSF>2.0.CO;2
- 896 Bosveld, F.C., 1997. Derivation of fluxes from profiles over a moderately homogeneous forest.
 897 *Boundary-Layer Meteorol.* 84, 289–327. doi:10.1023/A:1000453629876
- 898 Bou-Zeid, E., Parlange, M.B., Meneveau, C., 2007. On the parameterization of surface roughness at
 899 regional scales. *J. Atmos. Sci.* 64, 216–227. doi:10.1175/JAS3826.1
- 900 Businger, J.A., Wyngaard, J.C., Izumi, Y., Bradley, E.F., 1971. Flux-profile relationships in the
 901 atmospheric surface layer. *J. Atmos. Sci.* doi:10.1175/1520-
 902 0469(1971)028<0181:FPRITA>2.0.CO;2
- 903 Calaf, M., Higgins, C., Parlange, M.B., 2014. Large wind farms and the scalar flux over an
 904 heterogeneously rough land surface. *Boundary-Layer Meteorol.* 153, 471–495.
 905 doi:10.1007/s10546-014-9959-6
- 906 Cheng, H., Castro, I.P., 2002. Near-wall flow development after a step change in surface roughness.
 907 *Boundary-Layer Meteorol.* 105, 411–432. doi:10.1023/A:1020355306788

- 908 Cheng, Y., Brutsaert, W., 2005. Flux-profile relationships for wind speed and temperature in the
909 stable atmospheric boundary layer. *Boundary-Layer Meteorol.* 114, 519–538.
- 910 Cheng, Y., Parlange, M.B., Brutsaert, W., 2005. Pathology of Monin-Obukhov similarity in the
911 stable boundary layer. *J. Geophys. Res. Atmos.* 110, D06101. doi:10.1029/2004JD004923
- 912 Conangla, L., Cuxart, J., Soler, M.R., 2008. Characterisation of the nocturnal boundary layer at a
913 site in Northern Spain. *Boundary-Layer Meteorol.* 128, 255–276. doi:10.1007/s10546-008-
914 9280-3
- 915 de Franceschi, M., Zardi, D., Tagliazucca, M., Tampieri, F., 2009. Analysis of second-order
916 moments in surface layer turbulence in an Alpine valley. *Q. J. R. Meteorol. Soc.* 135, 1750–
917 1765. doi:10.1002/qj.506
- 918 Dellwik, E., Jensen, N.O., 2005. Flux–Profile relationships over a fetch limited beech forest.
919 *Boundary-Layer Meteorol.* 115, 179–204. doi:10.1007/s10546-004-3808-y
- 920 Derbyshire, S.H., 1995. Stable boundary layers: Observations, models and variability part I:
921 Modelling and measurements. *Boundary-Layer Meteorol.* 74, 19–54.
- 922 Dyer, A.J., 1974. A review of flux-profile relationships. *Boundary-Layer Meteorol.* 7, 363–372.
923 doi:10.1007/BF00240838
- 924 Finnigan, J., 2000. Turbulence in plant canopies. *Annu. Rev. Fluid Mech.* 32, 519–571.
925 doi:10.2480/agrmet.20.1
- 926 Finnigan, J.J., Shaw, R.H., 2000. A wind-tunnel study of airflow in waving wheat: an EOF analysis
927 of the structure of the large-eddy motion. *Boundary-layer Meteorol.* 96, 211–255.
928 doi:10.1023/A:1002618621171
- 929 Foken, T., 2008. *Micrometeorology*. Springer-Verlag Berlin Heidelberg.
- 930 Foken, T., Wichura, B., 1996. Tools for quality assessment of surface-based flux measurements.
931 *Agric. For. Meteorol.* 78, 83–105.
- 932 Forrer, J., Rotach, M.W., 1997. On the turbulence structure in the stable boundary layer over the
933 greenland ice sheet. *Boudary-Layer Meteorology* 85, 111–136.
- 934 Fortuniak, K., Pawlak, W., Siedlecki, M., 2013. Integral turbulence statistics over a Central
935 European city Centre. *Boundary-Layer Meteorol.* 146, 257–276. doi:10.1007/s10546-012-
936 9762-1
- 937 Grachev, A.A., Andreas, E.L., Fairall, C.W., Guest, P.S., Persson, P.O.G., 2015. Similarity theory
938 based on the Dougherty-Ozmidov length scale. *Q. J. R. Meteorol. Soc.* 141, 1845–1856.
939 doi:10.1002/qj.2488
- 940 Grachev, A.A., Andreas, E.L., Fairall, C.W., Guest, P.S., Persson, P.O.G., 2013. The critical
941 Richardson number and limits of applicability of local similarity theory in the stable boundary
942 layer. *Boundary-Layer Meteorol.* 147, 51–82. doi:10.1007/s10546-012-9771-0
- 943 Grachev, A.A., Andreas, E.L., Fairall, C.W., Guest, P.S., Persson, P.O.G., 2007. SHEBA flux-
944 profile relationships in the stable atmospheric boundary layer. *Boundary-Layer Meteorol.* 124,
945 315–333. doi:10.1007/s10546-007-9177-6
- 946 Ha, K.-J., Hyun, Y.-K., Oh, H.-M., Kim, K.-E., Mahrt, L., 2007. Evaluation of boundary layer
947 similarity theory for stable conditions in CASES-99. *Mon. Weather Rev.* 135, 3474–3483.
948 doi:10.1175/MWR3488.1
- 949 Harman, I.N., Finnigan, J.J., 2010. Flow over hills covered by a plant canopy: Extension to
950 generalised two-dimensional topography. *Boundary-Layer Meteorol.* 135, 51–65.
951 doi:10.1007/s10546-009-9458-3
- 952 Hicks, B., 1978. Some limitations of dimensional analysis and power laws. *Boundary-Layer*
953 *Meteorol* 14, 567–569. doi:10.1007/BF00121895
- 954 Högström, U., 1988. Non-dimensional wind and temperature profiles in the atmospheric surface
955 layer: A re-evaluation. *Boundary-Layer Meteorol.* 42, 55–78. doi:10.1007/BF00119875
- 956 Högström, U., Bergström, H., Smedman, A.S., Halldin, S., Lindroth, A., 1989. Turbulent exchange
957 above a pine forest, I: Fluxes and gradients. *Boundary-Layer Meteorol.* 49, 197–217.
958 doi:10.1007/BF00116411
- 959 Holtslag, A.A.M., Nieuwstadt, F.T.M., 1986. Scaling the atmospheric boundary layer. *Boundary-*

960 Layer Meteorol. 36, 201–209. doi:10.1007/BF00117468

961 Howell, J., Mahrt, L., 1997. Multiresolution flux decomposition. *Boundary-Layer Meteorol.* 83,

962 117–137. doi:10.1023/A:1000210427798

963 Howell, J.F., Sun, J., 1999. Surface-layer fluxes in stable conditions. *Boundary-Layer Meteorol.* 90,

964 495–520. doi:10.1023/A:1001788515355

965 Kaimal, J.C., 1973. Turbulence spectra, length scales and structure parameters in the stable surface

966 layer. *Boundary-Layer Meteorol.* 4, 289–309. doi:10.1007/BF02265239

967 Kaimal, J.C., Finnigan, J.J., 1994. *Atmospheric boundary layer flows: Their structure and*

968 *measurement.* University Press, New York.

969 Kaimal, J.C., Wyngaard, J.C., 1990. The Kansas and Minnesota Experiments. *Boundary-Layer*

970 *Meteorology* 50, 31–47.

971 Katul, G., Goltz, S.M., Hsieh, C.-I., Cheng, Y., Mowry, F., Sigmon, J., 1995. Estimation of surface

972 heat and momentum fluxes using the flux-variance method above uniform and non-uniform

973 terrain. *Boundary-Layer Meteorol.* 74, 237–260. doi:10.1007/BF00712120

974 Katul, G., Hsieh, C.I., Bowling, D., Clark, K., Shurpali, N., Turnipseed, A., Albertson, J., Tu, K.,

975 Hollinger, D., Evans, B., Offerle, B., Anderson, D., Ellsworth, D., Vogel, C., Oren, R., 1999.

976 Spatial variability of turbulent fluxes in the roughness sublayer of an even-aged pine forest.

977 *Boundary-Layer Meteorol.* 93, 1–28. doi:10.1023/A:1002079602069

978 Klipp, C.L., Mahrt, L., 2004. Flux-gradient relationship, self-correlation and intermittency in the

979 stable boundary layer. *Q. J. R. Meteorol. Soc.* 130, 2087–2103. doi:10.1256/qj.03.161

980 Kljun, N., Calanca, P., Rotach, M.W., Schmid, H.P., 2015. A simple two-dimensional

981 parameterisation for Flux Footprint Prediction (FFP). *Geosci. Model Dev.* 8, 3695–3713.

982 doi:10.5194/gmd-8-3695-2015

983 Kral, S.T., Sjöblom, A., Nygård, T., 2014. Observations of summer turbulent surface fluxes in a

984 High Arctic fjord. *Q. J. R. Meteorol. Soc.* 140, 666–675. doi:10.1002/qj.2167

985 Mahrt, L., 2014. Stably stratified atmospheric boundary layers. *Annu. Rev. Fluid Mech.* 46, 23–45.

986 doi:10.1146/annurev-fluid-010313-141354

987 Mahrt, L., 2011. The near-calm stable boundary layer. *Boundary-Layer Meteorol.* 140, 343–360.

988 doi:10.1007/s10546-011-9616-2

989 Mahrt, L., 2007. The influence of nonstationarity on the turbulent flux-gradient relationship for

990 stable stratification. *Boundary-Layer Meteorol.* 125, 245–264. doi:10.1007/s10546-007-9154-0

991 Mahrt, L., 2000. Surface heterogeneity and vertical structure of the boundary layer. *Boundary-*

992 *Layer Meteorol.* 96, 33–62. doi:10.1023/A:1002482332477

993 Mahrt, L., Thomas, C., Richardson, S., Seaman, N., Stauffer, D., Zeeman, M., 2013. Non-stationary

994 generation of weak turbulence for very stable and weak-wind conditions. *Boundary-Layer*

995 *Meteorol.* 147, 179–199. doi:10.1007/s10546-012-9782-x

996 Mahrt, L., Vickers, D., Frederickson, P., Davidson, K., Smedman, A.-S., 2003. Sea-surface

997 aerodynamic roughness. *J. Geophys. Res.* 108(C6), 3171. doi:10.1029/2002JC001383

998 Malhi, Y., 1996. The behaviour of the roughness length for temperature over heterogeneous

999 surfaces. *Q. J. R. Meteorol. Soc.* 122, 1095–1125.

1000 Marques Filho, E.P., Sá, L.D.A., Karam, H.A., Alvalá, R.C.S., Souza, A., Pereira, M.M.R., 2008.

1001 Atmospheric surface layer characteristics of turbulence above the Pantanal wetland regarding

1002 the similarity theory. *Agric. For. Meteorol.* 148, 883–892.

1003 doi:10.1016/j.agrformet.2007.12.004

1004 Martins, C.A., Moraes, O.L.L., Acevedo, O.C., Degrazia, G.A., 2009. Turbulence intensity

1005 parameters over a very complex terrain. *Boundary-Layer Meteorol.* 133, 35–45.

1006 doi:10.1007/s10546-009-9413-3

1007 Miller, N.E., Stoll, R., 2013. Surface heterogeneity effects on regional-scale fluxes in the stable

1008 boundary layer: Aerodynamic roughness length transitions. *Boundary-Layer Meteorol.* 149,

1009 277–301. doi:10.1007/s10546-013-9839-5

1010 Mironov, D. V., Sullivan, P.P., 2010. Effect of horizontal surface temperature heterogeneity on

1011 turbulent mixing in the stably stratified atmospheric boundary layer. *19th Amer. Meteorol.*

- 1012 Soc. Symp. Bound. Layers Turbul. CO, USA, 10 pp.
- 1013 Mölder, M., Grelle, A., Lindroth, A., Halldin, S., 1999. Flux-profile relationships over a boreal
1014 forest - Roughness sublayer corrections. *Agric. For. Meteorol.* 98-99, 645–658.
1015 doi:10.1016/S0168-1923(99)00131-8
- 1016 Monin, A.S., Obukhov, A.M., 1954. Basic laws of turbulent mixing in the surface layer of the
1017 atmosphere. *Contrib. Geophys. Inst. Acad. Sci. USSR* 24, 163–187.
- 1018 Monteith, J.L., Unsworth, M.H., 1990. *Principles of Environmental Physics*, 2nd ed. Edward
1019 Arnold, London.
- 1020 Moraes, O.L.L., Acevedo, O.C., Degrazia, G.A., Anfossi, D., da Silva, R., Anabor, V., 2005.
1021 Surface layer turbulence parameters over a complex terrain. *Atmos. Environ.* 39, 3103–3112.
1022 doi:10.1016/j.atmosenv.2005.01.046
- 1023 Nadeau, D.F., Pardyjak, E.R., Higgins, C.W., Parlange, M.B., 2013. Similarity scaling over a steep
1024 alpine slope. *Boundary-Layer Meteorol.* 147, 401–419. doi:10.1007/s10546-012-9787-5
- 1025 Nakamura, R., Mahrt, L., 2001. Similarity theory for local and spatially averaged momentum
1026 fluxes. *Agric. For. Meteorol.* 108, 265–279.
- 1027 Nieuwstadt, F.T.M., 1984. The turbulent structure of the stable, nocturnal boundary layer. *J. Atmos.*
1028 *Sci.* doi:10.1175/1520-0469(1984)041<2202:TTSOTS>2.0.CO;2
- 1029 Obukhov, A.M., 1946. Turbulence in an atmosphere with a non-uniform temperature. *Boundary-*
1030 *Layer Meteorol.* 2, 7–29.
- 1031 Pahlow, M., Parlange, M.B., Porté-Agel, F., 2001. On Monin–Obukhov similarity in the stable
1032 atmospheric boundary layer. *Boundary-Layer Meteorol.* 99, 225–248.
- 1033 Panofsky, H.A., Dutton, J.A., 1984. *Atmospheric Turbulence: Models and Methods for*
1034 *Engineering Applications*. John Wiley and Sons, New York.
- 1035 Rannik, Ü., 1998. On the surface layer similarity at a complex forest site. *J. Geophys. Res.* 103,
1036 8685–8697.
- 1037 Raupach, M.R., 1994. Simplified expressions for vegetation roughness length and zero-plane
1038 displacement as function of canopy height and area index. *Boundary-Layer Meteorol.* 71, 211–
1039 216.
- 1040 Raupach, M.R., 1979. Anomalies in flux-gradient relationships over forest. *Boundary-Layer*
1041 *Meteorol.* 16, 467–486.
- 1042 Raupach, M.R., Finnigan, J.J., Brunet, Y., 1996. Coherent eddies and turbulence in vegetation
1043 canopies: The mixing-layer analogy. *Boundary-Layer Meteorol.* 78, 351–382.
- 1044 Rotach, M.W., 1993. Turbulence close to a rough urban surface. Part II: Variances and gradients.
1045 *Boundary-Layer Meteorol.* 66, 75–92.
- 1046 Rotach, M.W., Andretta, M., Calanca, P., Weigel, A.P., Weiss, A., 2008. Boundary layer
1047 characteristics and turbulent exchange mechanisms in highly complex terrain. *Acta Geophys.*
1048 56, 194–219. doi:10.2478/s11600-007-0043-1
- 1049 Rotach, M.W., Calanca, P., 2014. *Microclimate*. Academic Press, pp. 258–264.
- 1050 Rotach, M.W., Calanca, P., Graziani, P., Gurtz, J., Steyn, D.G., Vogt, R., Andretta, M., Christen,
1051 A., Cieslik, S., Connolly, R., De Wekker, S.F.J. and Galmarini, S., Kadygrov, E.N.,
1052 Kadygrov, V., Miller, E., Neininger, B., Rucker, M., van Gorsel, E., Weber, H., Weiss, A.,
1053 Zappa, M., 2004. Turbulence structure and exchange processes in an Alpine Valley: The
1054 Riviera project. *Bull. Am. Meteorol. Soc.* 85, 1367–1385. doi:10.1175/BAMS-85-9-1367
- 1055 Sanz Rodrigo, J., Anderson, P.S., 2013. Investigation of the stable atmospheric boundary layer at
1056 Halley Antarctica. *Boundary-Layer Meteorology* 148, 517–539. doi:10.1007/s10546-013-9831-0
- 1057 Shaw, R.H., Finnigan, J.J., Patton, E.G., 2006. Eddy structure near the plant canopy interface. 17th
1058 Symp. Bound. Layers Turbul. J2.1.
- 1059 Simpson, I.J., Thurtell, G.W., Neumann, H.H., Den Hartog, G., Edwards, G.C., 1998. The validity
1060 of similarity theory in the roughness sublayer above forests. *Boundary-Layer Meteorol.* 87,
1061 69–99. doi:10.1023/A:1000809902980
- 1062 Sorbjan, Z., Grachev, A.A., 2010. An evaluation of the flux – gradient relationship in the stable
1063 boundary layer. *Boundary-Layer Meteorol.* 135, 385–405. doi:10.1007/s10546-010-9482-3

1064 Stiperski, I., Rotach, M.W., 2016. On the measurement of turbulence over complex mountainous
1065 terrain. *Boundary-Layer Meteorol.* 159, 97–121. doi:10.1007/s10546-015-0115-8

1066 Stoll, R., Porté-Agel, F., 2008. Large-eddy simulation of the stable atmospheric boundary layer
1067 using dynamic models with different averaging schemes. *Boundary-Layer Meteorol.* 126, 1–
1068 28. doi:10.1007/s10546-007-9207-4

1069 Stull, R.B., 1988. *An Introduction to Boundary-Layer Meteorology*. Kluwer Academic Publishers,
1070 Dordrecht.

1071 Thom, A.S., Stewart, J.B., Oliver, H.R., Gash, J.H.C., 1975. Comparison of aerodynamic and
1072 energy budget estimates of fluxes over a pine forest. *Q. J. R. Meteorol. Soc.* 101, 93–105.
1073 doi:10.1002/qj.49710142708

1074 Trini Castelli, S., Falabino, S., 2013. Analysis of the parameterization for the wind-velocity
1075 fluctuation standard deviations in the surface layer in low-wind conditions. *Meteorol. Atmos.*
1076 *Phys.* 119, 91–107. doi:10.1007/s00703-012-0219-3

1077 Večenaj, Ž., De Wekker, S.F.J., 2015. Determination of non-stationarity in the surface layer during
1078 the T-REX experiment. *Q. J. R. Meteorol. Soc.* 141, 1560–1571. doi:10.1002/qj.2458

1079 Vickers, D., Mahrt, L., 2003. The cospectral gap and turbulent flux calculations. *J. Atmos. Ocean.*
1080 *Technol.* 20, 660–672. doi:10.1175/1520-0426(2003)20<660:TCGATF>2.0.CO;2

1081 Wilczak, J., Oncley, S., Stage, S., 2001. Sonic anemometer tilt correction algorithms. *Boundary-*
1082 *Layer Meteorol.* 99, 127–150. doi:10.1023/A:1018966204465

1083 Wood, C.R., Lacser, A., Barlow, J.F., Padhra, A., Belcher, S.E., Nemitz, E., Helfter, C., Famulari,
1084 D., Grimmond, C.S.B., 2010. Turbulent flow at 190 m height above London during 2006-
1085 2008: A climatology and the applicability of similarity theory. *Boundary-Layer Meteorol.* 137,
1086 77–96. doi:10.1007/s10546-010-9516-x

1087 Wyngaard, J.C., Coté, O.R., 1972. Cospectral similarity in the atmospheric surface layer. *Q. J. R.*
1088 *Meteorol. Soc.* 98, 590–603. doi:10.1002/qj.49709841708

1089

1090